



Osteoblastic Swedish mutant APP expedites brain deficits by inducing endoplasmic reticulum stress-driven senescence

Jin-Xiu Pan^{1,2,3}, Dong Sun^{1,3}, Daehoon Lee^{1,2}, Lei Xiong^{1,2}, Xiao Ren¹, Hao-han Guo¹, Ling-Ling Yao¹, Yuyi Lu¹, Caroline Jung¹ & Wen-Cheng Xiong^{1,2}  

Patients with Alzheimer's disease (AD) often have osteoporosis or osteopenia. However, their direct link and relationship remain largely unclear. Previous studies have detected osteoporotic deficits in young adult *Tg2576* and *TgAPP_{swe}^{OCN}* mice, which express APP_{swe} (Swedish mutant) ubiquitously and selectively in osteoblast (OB)-lineage cells. This raises the question, whether osteoblastic APP_{swe} contributes to AD development. Here, we provide evidence that *TgAPP_{swe}^{OCN}* mice also exhibit AD-relevant brain pathologies and behavior phenotypes. Some brain pathologies include age-dependent and regional-selective increases in glial activation and pro-inflammatory cytokines, which are accompanied by behavioral phenotypes such as anxiety, depression, and altered learning and memory. Further cellular studies suggest that APP_{swe}, but not APP_{wt} or APP_{lon} (London mutant), in OB-lineage cells induces endoplasmic reticulum-stress driven senescence, driving systemic and cortex inflammation as well as behavioral changes in 6-month-old *TgAPP_{swe}^{OCN}* mice. These results therefore reveal an unrecognized function of osteoblastic APP_{swe} to brain axis in AD development.

¹Department of Neurosciences, School of Medicine, Case Western Reserve University, Cleveland, OH, USA. ²Louis Stokes Cleveland Veterans Affairs Medical Center, Cleveland, OH, USA. ³These authors contributed equally: Jin-Xiu Pan, Dong Sun. ✉email: Wen-Cheng.Xiong@case.edu

Alzheimer's disease (AD) is the most common form of dementia. It is pathologically characterized by cortical and cerebrovascular β -amyloid ($A\beta$) plaques, phosphor-tau containing neurofibrillary tangles, reactive glial cell (astrocyte and microglial cell)-associated chronic brain inflammation, and neuron-loss^{1,2}. Interestingly, in addition to brain pathologies, patients with AD, both early and late onset, often have osteopenia or osteoporosis^{3–10}, a condition characterized by the loss of bone-mass or bone mineral density (BMD) with micro-architectural deterioration of bone tissue, and a higher rate of hip fracture. However, little is known regarding the underlying mechanisms of AD association with bone loss.

A growing list of genetic risk genes has been identified in patients with early onset and late onset AD. Intriguingly, many of the AD risk genes, such as *TREM2* (triggering receptors expressed on myeloid cells-2) and *PYK2*, are highly expressed in immune cells and bone cells, and encode proteins that regulate not only neuron synaptic functions, but also immune responses and bone homeostasis^{11–15}. *APOE*, another AD risk gene, is also identified as a risk factor for osteoporosis^{16–18}. Among the various risk genes for AD development, we chose Swedish mutant APP (*APP_{swe}*) to address the question regarding AD association with bone loss for the following reasons. The Swedish mutations in the *APP* gene are initially identified in patients with early-onset (EO) AD, which promote the generation of $A\beta$ by favoring its proteolytic cleavage performed by β - and γ -secretases^{19–21}. Much research has focused on the impacts of $A\beta$ on the brain, even though *APP* or *APP_{swe}* is known to be expressed not only in the brain, but also in periphery tissues, including osteoblast (OB)-lineage cells^{22,23}. Although *APP_{swe}* is only detected in a small fraction of AD patients, it is commonly used to generate AD animal models, such as *Tg2576* and *5XFAD*^{24,25}. *APP_{swe}* in these animal models (in particularly *Tg2576*) is expressed ubiquitously, in both the brain and periphery tissues, including OB cells^{22,23}. While investigating the phenotypes of these *APP_{swe}*-based animal models have provided valuable insights into $A\beta$ brain pathology and impairments in mouse cognitive functions, the function of *APP_{swe}* in peripheral tissues, such as OBs, remains poorly understood. Previous examinations of bone structures in *Tg2576* mice have identified early-onset osteoporotic deficits, months before any brain-pathologic defect that was detected^{22,23}. Knocking out *App* (in *APP^{-/-}* mice), or selective expressing *APP_{swe}* in osteocalcin (OCN) promoter driven Cre (*OCN-Cre*)⁺ OB-lineage cells (in *TgAPP_{swe}^{OCN}* mice) recapitulates the osteoporotic defects in *Tg2576* mice^{23,26}. These observations raise an interesting question, could problems in the bone cells conversely contribute to AD pathology in the brain?

Here, we provide evidence that *TgAPP_{swe}^{OCN}* mice express *APP_{swe}* largely in the OB-lineage cells, with little to weak expression in the dorsal dentate gyrus (dDG) of the hippocampus. These mice develop age-dependent [starting at 6-month-old (MO)] and brain-region selective pathologies, and exhibit anxiety- and depression-like behaviors, as well as altered cognitive functions. While these mice at 6-MO showed brain-pathology (including glial activations and elevated pro-inflammatory cytokines) largely in the cortex, these mice at 12-MO showed brain-pathology mainly detected in the hippocampus. Further mechanistic studies demonstrate that *APP_{swe}*, but not *APP_{wt}* or *APP_{Ion}* (London mutant), in OB-lineage cells increases endoplasmic reticulum (ER)-stress, senescence, and SASPs (senescence associated secretory phenotypes). Inhibition of ER-stress abolishes *APP_{swe}*-induced senescence, and suppression of senescence diminishes brain and behavioral phenotypes in 6-MO *TgAPP_{swe}^{OCN}* mice. Taken together, these observations suggest that *APP_{swe}* in OB-lineage cells contributes to the brain-region selective inflammation and glial activation and induces anxiety-

and depression-like behaviors in age-dependent manner, which are largely due to elevated OB-senescence, SASPs, and systemic inflammation. These results thus uncover a link between *APP_{swe}* in the OB-lineage cells and AD development.

Results

Selective *APP_{swe}* expression in OB-lineage cells in *TgAPP_{swe}^{OCN}* mice. To investigate osteoblastic *APP_{swe}*'s function in AD development, we took advantage of *TgAPP_{swe}^{OCN}* mice, in which human *APP_{swe}* expression in *LSL-hAPP_{swe}* mice depends on the removal of LSL by the *OCN-Cre* (Fig. 1a)²³. Although *OCN-Cre* mice express *Cre* primarily in mature/adult OB-lineage cells^{27,28}, our recent study showed *Cre* activity in neurons of dDG hippocampus, olfactory bulb, and cerebellum²⁹. Thus, it is important to verify *APP_{swe}*'s expression in bone cells and brain tissues of *TgAPP_{swe}^{OCN}* mice. Notice that the *hAPP_{swe}* protein was detected in the OB-lineage BMSCs (bone marrow stromal cells), but not in the hippocampus or cortex of the *TgAPP_{swe}^{OCN}* mice (6-MO) (Fig. 1b, c). We then asked if this is due to *hAPP_{swe}*'s cleavage (to produce $A\beta_{40}$ or $A\beta_{42}$) in the brain tissues. ELISA measuring human $A\beta_{40}$ and $A\beta_{42}$ levels showed little-to-no $A\beta$ increase in the hippocampus, cortex, or serum samples (Fig. 1d, e); but slight increases of both $A\beta_{40}$ and $A\beta_{42}$ in the OB-lineage cells, of *TgAPP_{swe}^{OCN}* mice (6-MO), as well as in the brain tissues and serum samples of 6-MO *Tg2576* mice (Fig. 1d, e). These results eliminate the possibility of β - and γ -cleavages of *hAPP_{swe}* in the brain of 6-MO *TgAPP_{swe}^{OCN}* mice, suggesting little *hAPP_{swe}* expression in the mutant brain at this age. We further tested this view by RT-PCR analysis of *hAPP_{swe}*'s transcripts in the mutant mice. Using specific primers for human *APP*, a weak *hAPP_{swe}* expression (~1.5 fold over control) was detected in the *TgAPP_{swe}^{OCN}* brain regions (e.g., hippocampus, olfactory bulb, and cerebellum) where *OCN-Cre* is expressed²⁹, but not in the *OCN-Cre* negative cortex (Fig. 1f). Notice that the *hAPP_{swe}*'s transcripts were much more abundant in the BMSCs (~70 fold over control) than in the brain (Fig. 1f), implying a much weaker *Cre* activity in neurons than in OB-lineage cells of the *OCN-Cre* mice. This viewpoint is consistent with the RT-PCR findings that *Cre* is expressed largely in the OB-lineage cells (~128 fold over control), weakly (~18 fold over control) in the hippocampus, and undetectable in the cortex of *OCN-Cre* mice (Fig. 1g). Taken together, these results suggest that the *hAPP_{swe}* is highly expressed in *OCN-Cre*⁺ OB-lineage cells, but little to weakly expressed in the *OCN-Cre*⁺ dDG, olfactory bulb, and cerebellum neurons, of *TgAPP_{swe}^{OCN}* mice.

Age-dependent and brain region-selective elevations in reactive astrocytes, microglial cells, and inflammatory cytokines, and an impairment in DG neurogenesis in *TgAPP_{swe}^{OCN}* mice. We then addressed whether *TgAPP_{swe}^{OCN}* mice exhibit any brain pathology that is similar to those of *APP_{swe}*-based AD animal models (e.g., *Tg2576*)^{24,25,32–34}, by performing the following studies.

First, we measured both $A\beta_{40}$ and $A\beta_{42}$ levels in the bone cells and brain tissues of *TgAPP_{swe}^{OCN}* mice at ages of not only 6-MO, but also 12-MO. Although little $A\beta_{40}$ or $A\beta_{42}$ levels were detected in 6-MO *TgAPP_{swe}^{OCN}* cortex and hippocampus (Fig. 1d, e), $A\beta_{42}$, but not $A\beta_{40}$, was slightly elevated in 12-MO *TgAPP_{swe}^{OCN}* hippocampus, but not cortex nor serum samples (Supplementary Fig. 1a, b). Additionally, little to no $A\beta$ plaque was detected in 12-MO *TgAPP_{swe}^{OCN}* bone and brain sections, in contrast from brain sections from *5XFAD* mice (4.5 MO) (Supplementary Fig. 1c–e). These findings support the view for a weak *hAPP_{swe}*/ $A\beta_{42}$ expression in 12-MO *TgAPP_{swe}^{OCN}* hippocampal DG neurons.

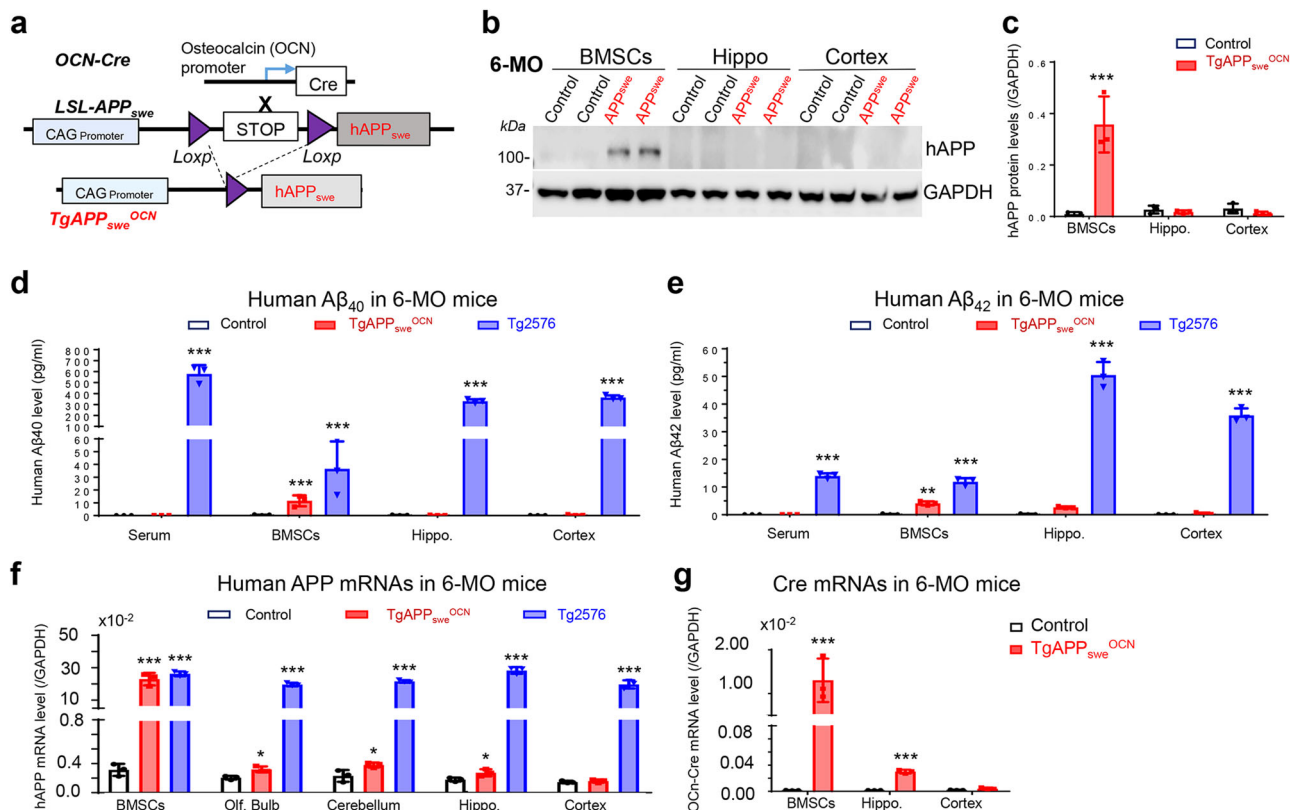


Fig. 1 Specific expression of APP_{swe} in OB-lineage cells in $TgAPP_{swe}^{OCN}$ mice. **a** Illustration of the transgene and generation of the conditional transgenic mice selectively expressing human APP_{swe} in an OCN-Cre dependent manner. **b, c** Western blot analysis of human APP (hAPP) protein levels in BMSCs, hippocampus, and cortex of 6-MO control ($LSL-APP_{swe}$) and $TgAPP_{swe}^{OCN}$ mice. **b** Representative blots; and **c** quantification. **d, e** ELISA analyses of human $A\beta_{40}$ (**d**) and $A\beta_{42}$ (**e**) levels in serum, BMSCs (50 μ g in total protein), and brain homogenates including hippocampus and cortex (300 μ g total protein) from 6-MO control, $TgAPP_{swe}^{OCN}$, and $Tg2576$ mice. **f** RT-PCR analysis of $hAPP$ gene expression in BMSCs, olfactory bulb, cerebellum, hippocampus, and cortex of 6-MO control and $TgAPP_{swe}^{OCN}$ mice. **g** RT-PCR analysis of Cre expression in BMSCs, hippocampus, and cortex of 6-MO control ($LSL-APP_{swe}$) and $TgAPP_{swe}^{OCN}$ mice. All data were presented as mean \pm SD. * $p < 0.05$, ** $p < 0.01$, *** $p < 0.001$ ($n = 3$ mice). Mann-Whitney U test was used in **c** and **g**, and one-way ANOVA followed by Tukey post hoc test was used in **d-f**.

Second, we examined neuronal distribution patterns and densities in the cortex and hippocampus of $TgAPP_{swe}^{OCN}$ mice (at age of ~7-MO) by conducting co-immunostaining analysis using antibodies against NeuN (a marker for all neurons) and Ctip2 (a marker for Layer V–VI neurons in the cortex and neurons in CA1-2 and DG). Little change in the NeuN⁺ and Ctip2⁺ neuron distribution patterns and densities was detected in $TgAPP_{swe}^{OCN}$ brains (Supplementary Fig. 2).

Third, we assessed the morphologies and densities of glial cells, including Olig2⁺ oligodendrocytes, S100 β ⁺ ependymal cells, GFAP⁺ astrocytes, and IBA1⁺ microglial cells, in the brain sections of control ($LSL-APP_{swe}$) and $TgAPP_{swe}^{OCN}$ mice. The Olig2⁺ oligodendrocytes and S100 β ⁺ ependymal cells appeared to be unchanged in the $TgAPP_{swe}^{OCN}$ cortex or brain (Supplementary Fig. 3). Intriguingly, both GFAP⁺ astrocytes and IBA1⁺ microglial cells were increased in 6-MO $TgAPP_{swe}^{OCN}$ cortex, particularly in layers I–III, but not in hippocampus (Fig. 2a–d), suggesting a brain region-selective activation of these glial cells. This view was further verified through a Western blot analysis, which showed increased GFAP and IBA1 protein levels in 6-MO $TgAPP_{swe}^{OCN}$ cortex, but not in hippocampus (Fig. 2e, f). Because glial cell activation is often associated with increased inflammation^{30,31}, we examined expressions of inflammation associated cytokines (e.g., *Il1b*, *Il6*, *Il10*, and *Tnfa*), growth factors (e.g., *Tgfb1* and *Csf2*), and proteinase (e.g., *Mmp3*) in both the cortex and hippocampus of control and $TgAPP_{swe}^{OCN}$ mice (at 6-MO) using RT-PCR analysis. The transcripts of *Il1b*, *Il10*, *Tnfa*,

and *Mmp3* were all increased in $TgAPP_{swe}^{OCN}$ cortex, but not in hippocampus (Fig. 2g, h), supporting the view of cortex as a vulnerable brain region in 6-MO $TgAPP_{swe}^{OCN}$ mice.

Fourth, we found that the glial activation and inflammatory phenotypes in $TgAPP_{swe}^{OCN}$ mice were not only brain-region selective, but also age-dependent. Whereas the cortex displayed the glial activation/inflammation in 6-MO $TgAPP_{swe}^{OCN}$ mice, these phenotypes were not detected in 3-MO $TgAPP_{swe}^{OCN}$ mice (Supplementary Fig. 4), but evidently more obvious in 12-MO $TgAPP_{swe}^{OCN}$ hippocampus than the cortex (Supplementary Fig. 5), suggesting age-dependent changes in the brain-region selectivity of the glial activation/inflammation phenotypes.

Finally, we examined adult neurogenesis in hippocampal DG (dentate gyrus), which is also impaired in AD animal models³². EdU was injected into the mice ~12 h before sacrifice to label proliferative neural stem cells (NSCs). Hippocampal sections were co-immunostained EdU with antibodies against DCX (doublecortin) (a marker for newborn neurons derived from NSCs). While $TgAPP_{swe}^{OCN}$ mice at 3-MO showed no difference in EdU⁺ and DCX⁺ cell densities compared to the controls, $TgAPP_{swe}^{OCN}$ mice at 6-MO displayed significant reductions in EdU⁺ and DCX⁺ cell densities at both dorsal and ventral DG (Supplementary Fig. 6), demonstrating an age-dependent impairment in the hippocampal DG neurogenesis of $TgAPP_{swe}^{OCN}$ mice, similar to that described in AD animal models³².

In aggregate, $TgAPP_{swe}^{OCN}$ mice (starting at 6-MO) exhibit partial AD relevant brain pathologies, which include increased

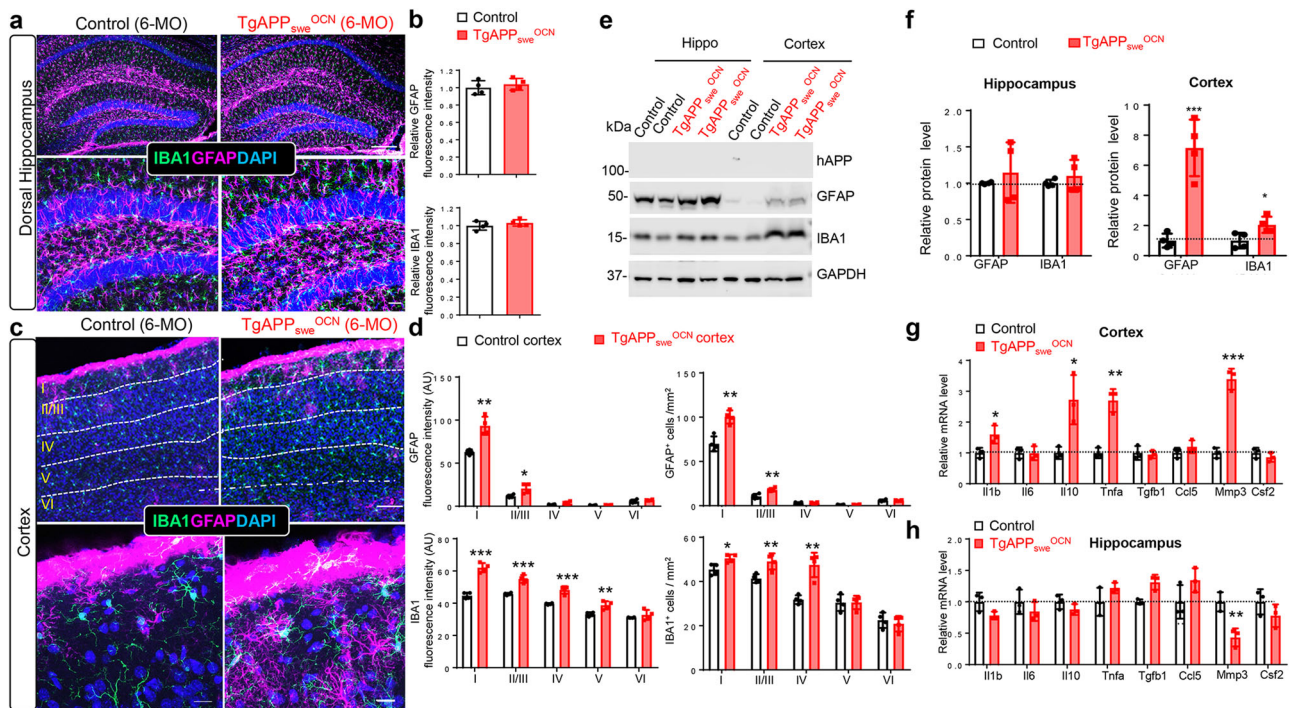


Fig. 2 Elevated reactive astrocytes, microglial cells, and inflammatory cytokines in 6-MO *TgAPP_{swe}^{OCN}* cortex, but not hippocampus. **a** Representative images of co-immunostaining with IBA1 (green), GFAP (magenta), and DAPI (blue) of hippocampal sections from 6-MO control (*LSL-APP_{swe}*) and *TgAPP_{swe}^{OCN}* mice. Scale bars: 200 μ m (upper) and 20 μ m (lower). **b** Quantification of data in **a**. **c** Representative images of co-immunostaining with IBA1 (green), GFAP (magenta), and DAPI (blue) of cortex sections from 6-MO control (*LSL-APP_{swe}*) and *TgAPP_{swe}^{OCN}* mice. Scale bars: 100 μ m (upper) and 20 μ m (lower). **d** Quantification of data in **c**. **e** Representative Western blots using antibodies against hAPP, GFAP, and IBA1 in homogenates of cortex and hippocampus of control and *TgAPP_{swe}^{OCN}* mice. GAPDH was used as a loading control. **f** Quantification of the data in **e**. **g–h** Real-time PCR (RT-PCR) analysis of indicated gene expressions in 6-MO control (*LSL-APP_{swe}*) and *TgAPP_{swe}^{OCN}* cortex (**g**) and hippocampus (**h**). All quantification data were presented as mean \pm SD ($n = 3–4$). * $p < 0.05$, ** $p < 0.01$, *** $p < 0.001$. Student's *t* test was used in **b**, **d**, and **f–h**.

reactive astrocytes, microglial cells, and inflammatory cytokines in the cortex (at 6-MO)/hippocampus (at 12-MO), impaired DG neurogenesis, and elevated $A\beta_{42}$ in 12-MO hippocampus.

Age-dependent anxiety- and depression-like behaviors in *TgAPP_{swe}^{OCN}* mice. Glial activation, brain inflammation, and decreased DG neurogenesis are often associated with depression- and/or anxiety-like behaviors^{33–38}. We thus subjected *TgAPP_{swe}^{OCN}* and control mice to an open field test (OFT) for evaluation of *TgAPP_{swe}^{OCN}* mice's anxiety and locomotor activity. *TgAPP_{swe}^{OCN}* mice at 6- and 12-MO, but not 3-MO, showed reduced center duration time but comparable total distance traveled to the controls (Fig. 3a, b and Supplementary Fig. 7a, b), suggesting a reduced exploratory, but not locomotor, activity, in the mutant mice, and implicating anxiety and/or depression. We further examined their behaviors using elevated plus maze test (EPMT) and light/dark transition test (LDT), both tests widely used to assess anxiety-related behavior in mouse models^{39,40}. Indeed, *TgAPP_{swe}^{OCN}* mice, again at 6- and 12-MO, but not 3-MO, showed decreased open arm duration time and entries by EPMT (Fig. 3c, d and Supplementary Fig. 7c, d), and reduced time in light box room in the LDT (Fig. 3e and Supplementary Fig. 7e), supporting the view for anxiety-like behaviors. We then assessed their depression-like behaviors using tail suspension test (TST), force swimming test (FST), and sucrose preference test (SPT). *TgAPP_{swe}^{OCN}* mice (6- and 12-MO, but not 3-MO) appeared to be depressed, exhibiting increased immobility times in both TST (Fig. 3f and Supplementary Fig. 7f) and FST (Fig. 3g and Supplementary Fig. 7g) and reduced sucrose preference (Fig. 3h and Supplementary

Fig. 7h). Together, these results suggest that *TgAPP_{swe}^{OCN}* mice experience age-dependent (starting at 6-MO) anxiety- and depression-like behaviors.

Since *hAPP_{swe}* is weakly expressed in dDG neurons in *TgAPP_{swe}^{OCN}* hippocampus (Fig. 1f), we wondered whether such a weak dDG expression of *APP_{swe}* could induce similar behavior phenotypes to that in *TgAPP_{swe}^{OCN}* mice. The AAV-CamkII-Cre (Cre under the control of CamkII promoter for excitatory neuron expression) and AAV-CamkII-GFP (as control) were specifically injected into the dDGs of both sides of the hippocampus in *LSL-APP_{swe}* mice (at age of 4-MO); and mice at 6-MO were subjected to the behavior tests (Supplementary Fig. 8a). While dDG neurons in *LSL-APP_{swe}* mice were successfully infected with the viruses (indicated by the GFP, *hAPP_{swe}* expression, and $A\beta_{42}$ increase) (Supplementary Fig. 8b–g), little to no differences in behavior tests using EMPT, LDT, TST, FST, and SPT were detected between Cre and GFP virus injected mice (Supplementary Fig. 8h–l), unlike the *TgAPP_{swe}^{OCN}* mice. These results thus implicate that the anxiety- or depression-like behaviors in 6-MO *TgAPP_{swe}^{OCN}* mice are in large due to *APP_{swe}*'s expression in OB-lineage cells, but not dDG neurons.

Age-dependent alterations in spatial learning and memory in *TgAPP_{swe}^{OCN}* mice. Although anxiety- and depression-like behaviors are present in AD animal models (e.g., *Tg2576* and *5XFAD*)^{41–43} and AD patients^{44–46}, a key AD relevant functional deficit is the age-dependent cognition decline^{47,48}. Therefore, we subjected *TgAPP_{swe}^{OCN}* and control (*LSL-APP_{swe}*) mice to the Morris water maze (MWM) test (to access mouse spatial learning and memory function)⁴⁹, and the novel object recognition (NOR)

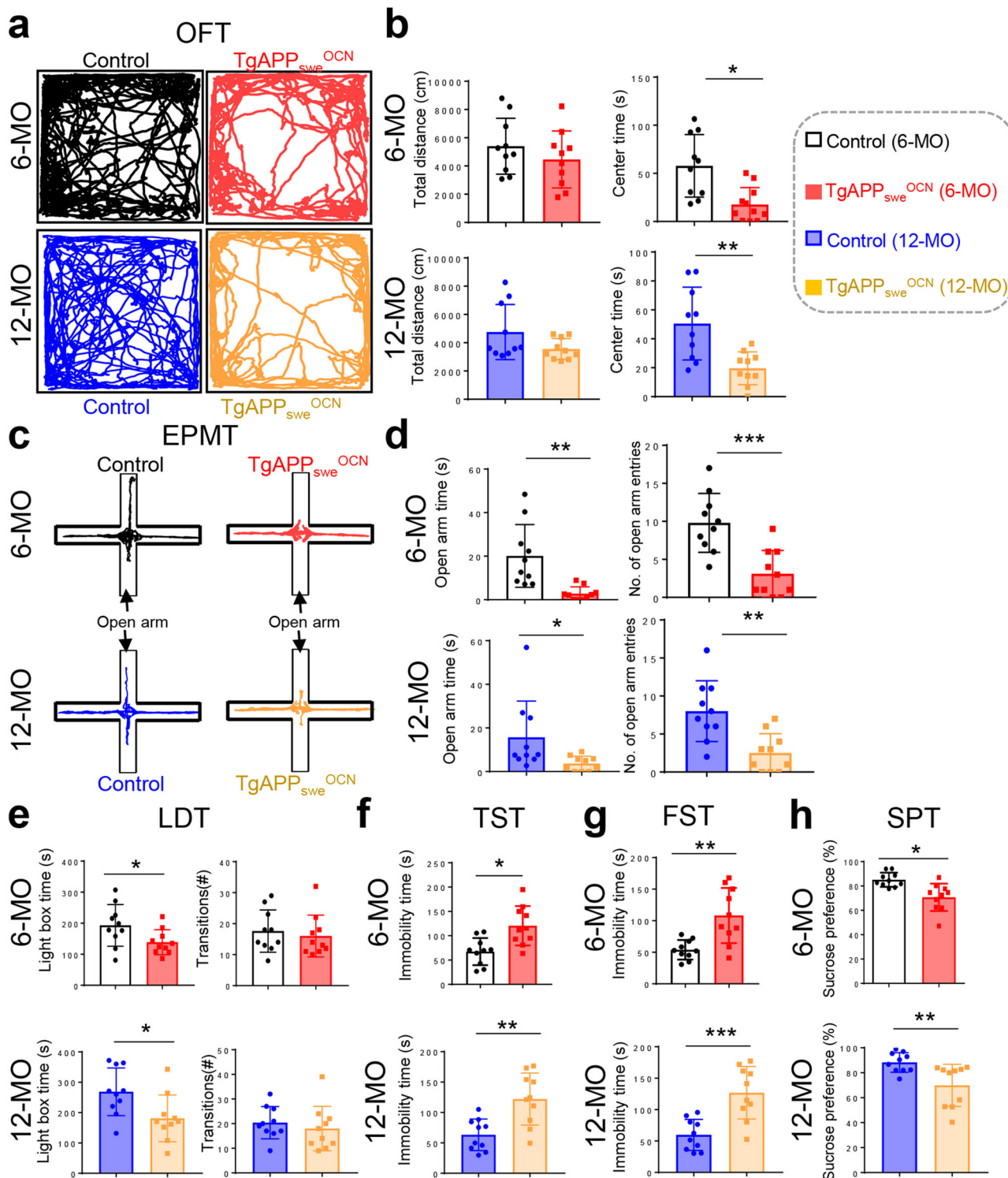


Fig. 3 Age-dependent anxiety- and depression-like behaviors in *TgAPP_{swe}^{OCN}* mice. **a, b** OFT: Representative tracing images (**a**), and quantifications of total distance and center duration time (**b**) were shown. **c, d** EPMT: Representative tracing images (**c**), and quantifications of open arm duration time and entries (**d**) were shown. **e** LDT: Quantifications of the time spent in the light room and the number of transitions into the light room. **f** TST, **g** FST, and **h** SPT. In all these behavior tests, 6-MO and 12-MO control (*LSL-APP_{swe}*) and *TgAPP_{swe}^{OCN}* mice (males) were examined. All quantification data were shown as mean ± SD (*n* = 10 mice). **p* < 0.05, ***p* < 0.01, ****p* < 0.001, Student's *t* test.

test (to evaluate mouse recognition memory)^{50,51}. Interestingly, age-dependent changes in both MWM and NOR tests were detected in *TgAPP_{swe}^{OCN}* mice. No obvious difference in MWM or NOR task performance was observed between *TgAPP_{swe}^{OCN}* and control mice at 3-MO (Fig. 4a–c). Un-expectedly, at 6-MO,

TgAPP_{swe}^{OCN} mice exhibited faster learning and better long-term memory in MWM (Fig. 4d, e), but no obvious difference in NOR task performance (Fig. 4f), compared to the age-matched controls, suggesting an improvement in spatial learning and memory in 6-MO *TgAPP_{swe}^{OCN}* mice. Interestingly, at ~12-MO,

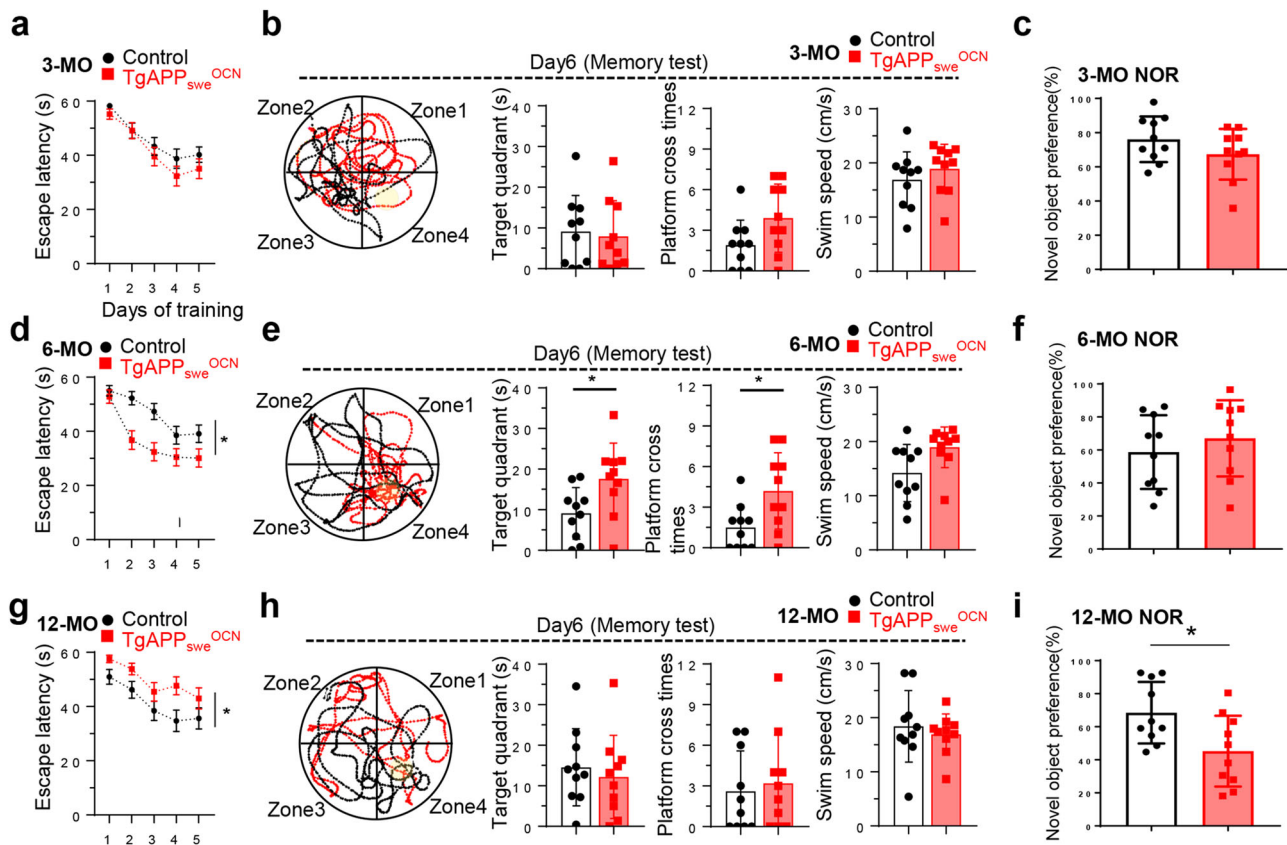


Fig. 4 Age-dependent alterations in spatial learning and memory in $TgAPP_{swe}^{OCN}$ mice. **a-c** 3-MO control ($LSL-APP_{swe}$) and $TgAPP_{swe}^{OCN}$ male mice were subject to Morris water maze (MWM) (**a, b**) and Novel Object Recognition (NOR) (**c**) tests. **d-f** 6-MO control ($LSL-APP_{swe}$) and $TgAPP_{swe}^{OCN}$ male mice were subject to MWM (**d, e**) and NOR (**f**) tests. **g-i** 12-MO control ($LSL-APP_{swe}$) and $TgAPP_{swe}^{OCN}$ male mice were subject to MWM (**g, h**) and NOR (**i**) tests. In MWM tests, the latencies to reach the hidden platform during the training period were showed in **a, d**, and **g**; and the representative tracing images and quantification of time spent in target quadrant, platform crossing time, and swim speed were shown in **b, e**, and **h**. In NOR tests, the time spent with novel object per total time with both objects as the novel object preference was quantified, shown in **c, f**, and **i**. All values were presented as mean \pm SD ($n = 10$ mice). * $p < 0.05$, one-way ANOVA followed by Tukey post hoc test was used in **a, d**, and **g**, and Student's t test was used in **b, c, e, f, h**, and **i**.

impairments in both MWM and NOR tasks were detected in $TgAPP_{swe}^{OCN}$ mice (Fig. 4g–i). These results are intriguing, demonstrating age-dependent changes in spatial and novel object learning and memory of $TgAPP_{swe}^{OCN}$ mice, in line with their age-dependent changes in the brain-region selectivity of the glial activation/inflammation.

Increased senescence and SASPs in APP_{swe}^{+} OB-lineage cells.

To investigate if and how APP_{swe} in $OCN-Cre^{+}$ OB-lineage cells gives rise to the brain and behavior phenotypes, we purified $OCN-Cre^{+}$ BMSCs (marked by $tdTomato^{+}$, believed to be OB progenitors²⁸) from both 6-MO control ($OCN-Cre; Ai9$) and $TgAPP_{swe}^{OCN}; Ai9$ mice using fluorescence-activated cell sorting (FACS), and then subjected them to RNA-seq analysis (Fig. 5a). 917 up- and 1825 down-regulated genes were identified in APP_{swe}^{+} OB progenitors (Fig. 5b). Among these genes, 154 up- and 269 down-regulated genes encode secreted proteins (Fig. 5b). Interestingly, GO analysis showed that most up-regulated genes are involved in inflammatory response, cytokine production, and cytokine/chemokine-mediated signaling pathways; and most down-regulated genes are implicated in cell cycle, cell proliferation, and bone mineralization (Fig. 5c). Further heat map analysis illustrated the up- and down-regulated genes for bone mass regulators, cytokines and chemokines, AD risk genes, and growth factors critical for neurogenesis (Fig. 5d). Some of these up/down regulated genes were verified by RT-PCR analyses (Fig. 5e).

Notice that transcription factors (e.g., *Sp7*, *Nfatc1*, *Satb2*, *Spp1*, *Sparc*, and *Jun*) for OB-lineage cell proliferation, differentiation, or mineralization, and bone-mass regulators (e.g., *Bmp2*, *Ihh*, *Lrp4*, and *Ctnnb1*) were down regulated in APP_{swe}^{+} OB progenitors (Fig. 5d, e), in line with our previous report²³, and some of the AD-risk genes including *Trem2*, *ApoE*, *Cd33*, *Sorl1*, *Vps35*, *Ptk2b*, and *Psen1/2* were altered in APP_{swe}^{+} OB progenitors, and growth factors including brain-derived neurotrophic factor (*Bdnf*) and insulin-like growth factor 1 (*Igf1*) were decreased in APP_{swe}^{+} OB progenitors (Fig. 5d, e).

Interestingly, the increased cytokines and chemokines exhibits features of SASPs^{52,53}. We thus asked if APP_{swe}^{+} OB-progenitors undergo senescence. Indeed, senescence marker proteins, such as SA- β -gal (senescence associated β -galactosidase), P16^{Ink4a}, P21, and P53^{54,55}, were all elevated in APP_{swe}^{+} OB-progenitors (derived from 3- and 6-MO mice) (Fig. 6), suggesting that APP_{swe} induces OB-senescence. We also detected reductions in $tdTomato^{+}$ (Td^{+}) or $OCN-Cre^{+}$ OB progenitors (Supplementary Fig. 9a, b) and in EdU^{+} proliferative cells in OB-progenitor cultures from $TgAPP_{swe}^{OCN}; Ai9$ mice (Supplementary Fig. 9c–e), indicating a growth arrest of these cells, another feature of cellular senescence in APP_{swe}^{+} OB-progenitors.

Finally, we wondered whether other tissues in $TgAPP_{swe}^{OCN}$ mice develop senescence-like phenotypes. The mRNAs from various tissues [including cortex, hippocampus, TA (Tibialis anterior) muscles, kidneys, and livers] of 6-MO control and $TgAPP_{swe}^{OCN}$

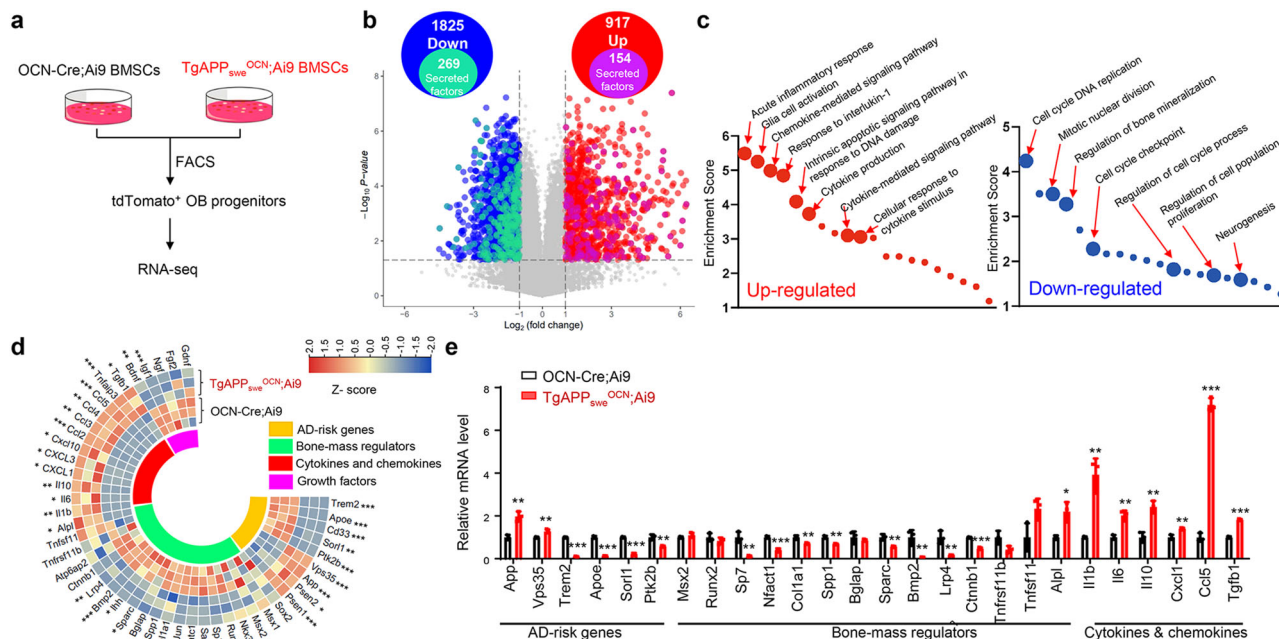


Fig. 5 Increased cytokines and chemokines in APP_{swe}^+ OB-progenitor cells. **a** Schematic of purification and RNA-seq of Tdtomato⁺ (Td⁺) OB progenitors from control (*OCN-Cre; Ai9*) and *TgAPP_{swe}^{OCN}; Ai9* mice. **b-d** Volcano plots (**b**), GO analysis of up/down-regulated genes (**c**), and heat map (**d**) of differentially expressed genes identified by RNA-seq. **e** RT-PCR analysis of AD risk gene *App*, *Vps35*, *Trem2*, *ApoE*, *Ptk2b*, and *Sor11*; bone-mass regulator *Sp7*, *Nfatc1*, *Col1a1*, *Spp1*, *Sparc*, *Bmp2*, *Lrp4*, and *Ctnnb1*; cytokine *Il1b*, *Il6*, and *Il10*; chemokine *Ccl5* and *Cxcl1*, growth factor *Tgfb1* gene expression in purified Td⁺ OB progenitors from 6-MO control (*OCN-Cre; Ai9*) and *TgAPP_{swe}^{OCN}; Ai9* mice. All values were presented as mean ± SD (*n* = 3 mice). **p* < 0.05, ***p* < 0.01, and ****p* < 0.001, by Mann-Whitney *U* test.

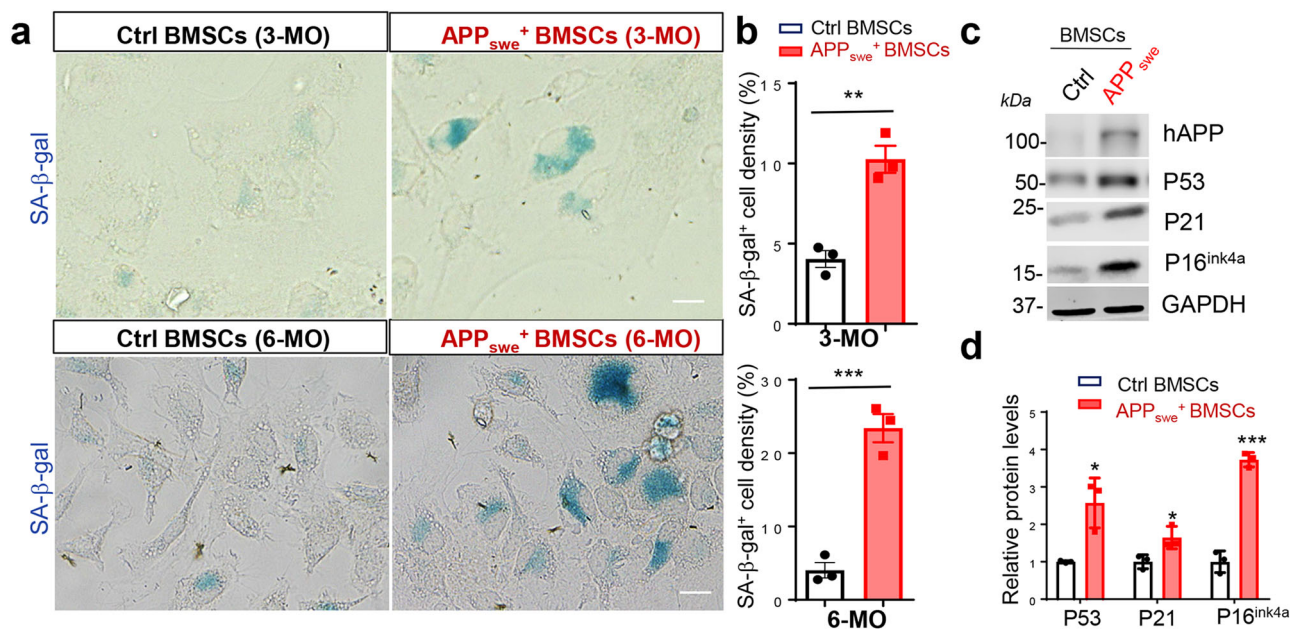


Fig. 6 Increased cellular senescence in APP_{swe}^+ OB-lineage cells. **a** SA-β-gal staining of 3-MO and 6-MO BMSCs from control (*LSL-APP_{swe}*) and *TgAPP_{swe}^{OCN}* mice. Scale bar, 20 μm. **b** Quantification of SA-β-gal⁺ cell densities (mean ± SD; *n* = 3 independent experiments). ***p* < 0.01, ****p* < 0.001. **c** Western blot analysis of indicated protein expression in BMSCs from mice with indicated genotypes (at 6-MO). GAPDH was used as a loading control. **d** Quantification analyses of the data in **c**, **p* < 0.05, ****p* < 0.001. mean ± SD *n* = 3. Mann-Whitney *U* test.

mice were subjected to RT-PCR analyses with *P16^{Ink4a}* and *P53* transcripts—both markers of senescence. Interestingly, both *P16^{Ink4a}* and *P53* were increased in the cortex and TA muscles, but not kidney or liver, of 6-MO *TgAPP_{swe}^{OCN}* mice (Supplementary Fig. 10a–e). These results suggest brain-region and tissue selective senescence-like phenotypes in *TgAPP_{swe}^{OCN}* mice.

Diminished behavior phenotypes and brain pathology in $TgAPP_{swe}^{OCN}$ mice treated with senescence inhibitor. To determine if the increased senescence and SASPs in *TgAPP_{swe}^{OCN}* mice contribute to the brain and behavior deficits, we treated *TgAPP_{swe}^{OCN}* mice with Dasatinib (D) + Quercetin (Q), or Veh control (10% PEG 400), because the

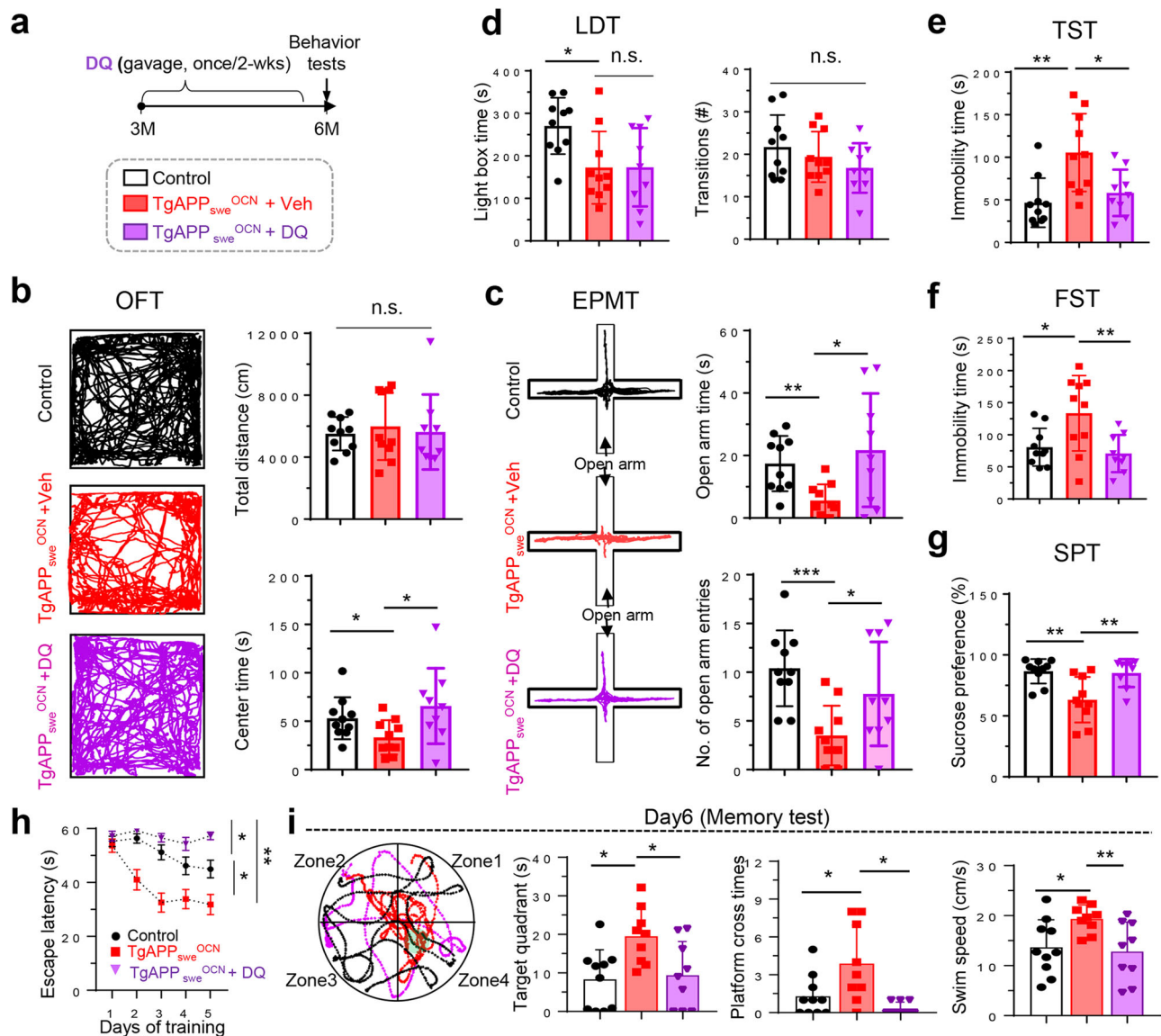


Fig. 7 Diminished behavior phenotypes in $TgAPP_{swe}^{OCN}$ mice treated with senescence inhibitors. **a** Schematic diagram of experimental design. 6-MO control ($LSL-APP_{swe}$, $n = 10$ males) and $TgAPP_{swe}^{OCN}$ mice were treated with Veh (10% PEG 400) ($n = 10$ males) or DQ (D 5 mg/kg, Q 50 mg/kg, dissolved in 10% PEG 400, once per two weeks) ($n = 9$ males), starting at age of 3-MO, and then subjected to indicated behavior tests at 6-MO. **b** OFT: Representative tracing images and quantifications of the total distance and the center duration time were shown. n.s. not significant, $*p < 0.05$. **c** EPMT: Representative tracing images and quantifications of the open arm duration time and entries were shown. $*p < 0.05$, $**p < 0.01$, $***p < 0.001$. **d** LDT: Quantifications of the time spent in the light room and the number of transitions into the light room were shown. n.s. not significant, $*p < 0.05$. **e** TST, **f** FST, and **g** SPT were shown. $*p < 0.05$, $**p < 0.01$. **h-i** MWM: the latency to reach the hidden platform during the training period (**h**), and representative tracing image and quantification of the time spent in the target quadrant, platform crossing time and swim speed (**i**) were shown. $*p < 0.05$, $**p < 0.01$. One-way ANOVA followed by Tukey post hoc test. All data were presented as mean \pm SD.

combination of D + Q is a well examined effective senolytic drug in animal studies^{56,57}. We first treated cultured OB progenitors (BMSCs) from $TgAPP_{swe}^{OCN}$ mice with D + Q. As expected, the senescence markers (SA- β -gal, P53, and P16^{Ink4a}) and the SASP-like factors (e.g., *Il1b*, *Il6*, *Cxcl1*, *Ccl5*, and *Tgfb1*) were all decreased in D + Q treated APP_{swe}^{OCN} OB-progenitors (Supplementary Fig. 11), verifying D + Q's inhibitory effects on OB-senescence. We then administered D + Q to $TgAPP_{swe}^{OCN}$ mice as illustrated in Fig. 7a. Remarkably, nearly all the behavior phenotypes, including depression (by TST, FST, and SPT), anxiety (by OFT and EPMT), and improved spatial learning and memory (by MWM) in $TgAPP_{swe}^{OCN}$ mice (at 6-MO) were all diminished by D + Q treatments (Fig. 7b–i), providing evidence for senescence as a

potential pathological mechanism for these behavior changes. Notice that D + Q treatments had little effect on the anxiety-like behavior assessed by LDT (Fig. 7d), implicating additional mechanism(s) underlying this event.

Moreover, the GFAP⁺ reactive astrocytes, IBA1⁺ cells, and SASP-like factors (e.g., *Il1b*, *Tnfa*, but not *Il10* or *Mmp3*) in $TgAPP_{swe}^{OCN}$ cortex were attenuated (Supplementary Fig. 12a–c), and the impaired hippocampal DG neurogenesis in $TgAPP_{swe}^{OCN}$ mice was restored (Supplementary Fig. 12d, e) by D + Q treatments. In aggregates, these results suggest that APP_{swe} -induced senescence and SASPs are likely to prompt cortical brain inflammation and glial activation, which may underlie the behavioral phenotypes in 6-MO $TgAPP_{swe}^{OCN}$ mice.

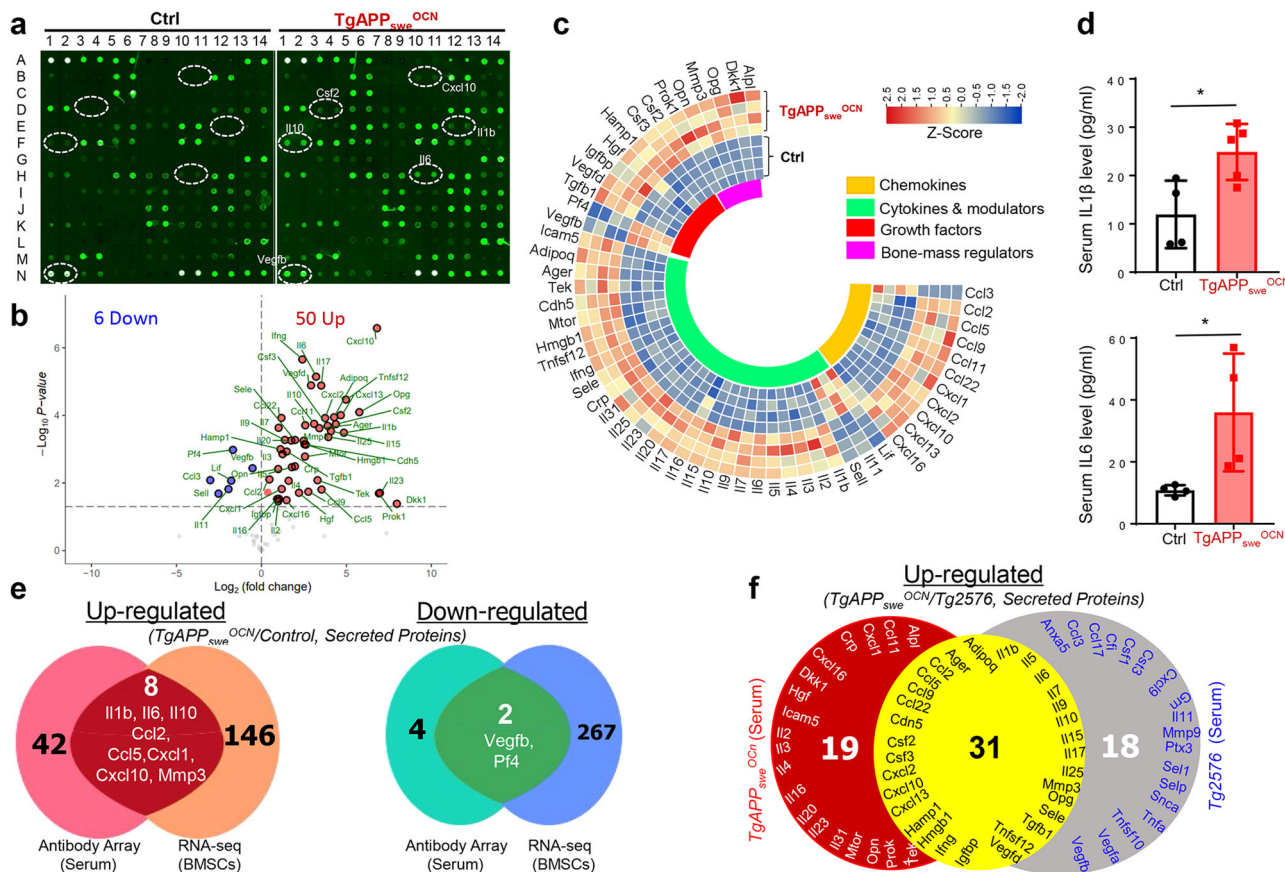


Fig. 8 Increased cytokines and chemokines in *TgAPP_{swe}^{OCN}* serum samples. **a** Representative images of serum L-Series label-multiplex antibody arrays of -7-MO control and *TgAPP_{swe}^{OCN}* mice. **b** Volcano plots analysis of **a**. **c** Heat map of data in **a**. $n = 4$, significant difference was set at $p < 0.05$. **d** Elisa assays of serum IL1β and IL6 levels in -7-MO control and *TgAPP_{swe}^{OCN}* mice. The data were presented as mean ± SD ($n = 4$ mice). * $p < 0.05$ by Student’s *t* test. **e** Comparison between this antibody array with secreted factors by RNA-seq of purified Tdtomato⁺ BMSCs. **f** Comparison of the changes (upregulated secreted proteins in Tg2576 over control mice) to those detected in *TgAPP_{swe}^{OCN}* mice.

Systemic inflammation in *TgAPP_{swe}^{OCN}* mice likely due to APP_{swe}-induced OB-senescence and SASPs. To further understand how APP_{swe}-induced OB-senescence and SASPs contribute to the brain pathology and behavior changes in *TgAPP_{swe}^{OCN}* mice, we speculate that APP_{swe} induced OB-senescence and SASPs contribute to systemic inflammation, which promotes brain inflammation and behavior changes. To test this speculation, we addressed the following questions.

First, are the increased SASPs (such as cytokines and chemokines) in APP_{swe}⁺ OB progenitors released and traveled through the circulation system of *TgAPP_{swe}^{OCN}* mice to induce the systemic inflammation? Using multiplexed antibody-based arrays to screen for altered serum/plasma proteins in *TgAPP_{swe}^{OCN}* mice (~7-MO) compared to their litter-mate control mice (*LSL-APP_{swe}*), increases in chemokines (CCL2, 5, 9, 11, 22, CXCL1, 2, 10, 13, 16), cytokines (IL1β, 2, 3, 4, 5, 6, 7, 9, 10, 15, 16, 17, 20, 23, 25, 31), and cytokine modulators (HMGB1, MTOR, CDH5) in the serum samples of *TgAPP_{swe}^{OCN}* mice (Fig. 8a–c), indicating a systemic inflammation. The increases in serum IL1β and IL6 levels in *TgAPP_{swe}^{OCN}* mice were verified by ELISA analyses (Fig. 8d). Notice that 8 up-regulated proteins (IL1β, 6, 10; CCL2, 5; CXCL1, 10 and MMP3) and 2 down-regulated proteins (VEGFB and PF4) were identified not only by the serum antibody array assay, but also by the RNA-seq analysis of OB progenitors (Fig. 8e), suggesting that many of the serum cytokines come from the APP_{swe}-induced OB-derived SASPs.

Second, is APP_{swe} in OCN-Cre⁺ cells a key contributor to the systemic inflammation? Although APP_{swe} is largely expressed in

OB-lineage cells of *TgAPP_{swe}^{OCN}* mice (Fig. 1), we cannot rule out the potential contribution of APP_{swe}’s weak expression in the hippocampal dDG to systemic inflammation. To this end, we examined the serum inflammatory cytokines and chemokines in mice (*LSL-APP_{swe}*) injected with AAV-CaMKII-Cre or AAV-GFP into their dDGs; and the Cre-injected mice exhibited similar levels of APP_{swe}/Aβ₄₂ in the hippocampus compared to 12-MO *TgAPP_{swe}^{OCN}* mice (Supplementary Fig. 8g). Using a small-scale antibody array containing antibodies against multiple SASP-like pro-inflammatory cytokines and chemokines (Supplementary Fig. 13a), little to no change was detected between the serum samples from the Cre and GFP injected mice (Supplementary Fig. 13a, b). These results thus eliminate the possibility of dDG APP_{swe}/Aβ₄₂ contribution to the systematic inflammation, supporting APP_{swe} in OCN-Cre⁺ OB-lineage cells as a major contributor of systemic inflammation. We also measured serum inflammatory factors in Tg2576 mice, a well-studied AD animal model that expresses APP_{swe} ubiquitously²⁴, using multiplexed antibody-based arrays, and compared the changes (upregulated secreted proteins in Tg2576 over control mice) with *TgAPP_{swe}^{OCN}* mice. Among 49 upregulated secreted proteins in Tg2576 mice, 31 (~63%) were increased in *TgAPP_{swe}^{OCN}* mice (Fig. 8f), providing additional support for the view.

Third, is the systemic inflammation results from the APP_{swe} induced-senescence and SASPs? Measuring serum SASP-like cytokines and chemokines in *TgAPP_{swe}^{OCN}* mice treated with and without D + Q, as illustrated in Fig. 7a, demonstrate that many cytokines (IL1β, 2, 23, 27) and chemokines (CCL2, 11 and

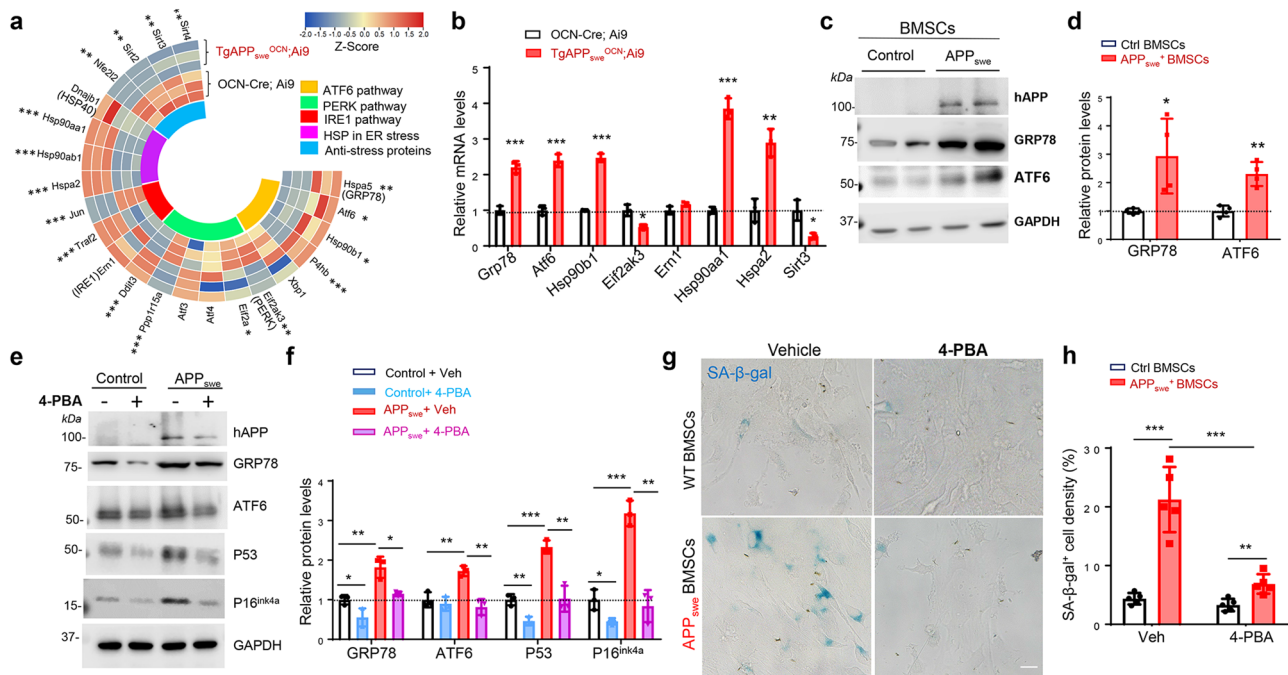


Fig. 9 **APP_{swe} induction of OB-senescence via ER stress.** **a** Heat map of differentially expressed ER stress or anti-stress related genes identified by RNA-seq in control (OCN-Cre; Ai9) and *TgAPP_{swe}^{OCN}; Ai9* Td⁺ OB-progenitors (detail analysis was described in Methods). **b** RT-PCR analysis of ER stress-related genes *Grp78*, *Atf6*, *Hsp90b1*, *Eif2ak3*, *Ern1*, *Hsp90aa1*, and *Hspa2* and anti-stress related gene *Sirt3* gene expression in purified Td⁺ BMSCs from 6-MO control (OCN-Cre; Ai9) and *TgAPP_{swe}^{OCN}; Ai9* mice, **p* < 0.05, ***p* < 0.01, ****p* < 0.001, mean ± SD, *n* = 3, Mann-Whitney U test. **c** Western blot analysis of indicated protein expression in BMSCs from mice with indicated genotypes (at 6-MO). GAPDH was used as a loading control. **d** Quantification of data in **c**, **p* < 0.05, ***p* < 0.01. mean ± SD, *n* = 4, Student's *t* test. **e** Western blot analysis in BMSCs from 6-MO control and *TgAPP_{swe}^{OCN}* with or without 0.25 mM 4-PBA (4-Phenylbutyric acid) treatment. **f** Quantification analyses of the data in **e**, **p* < 0.05, *n* = 3. **g** SA-β-gal staining of 6-MO control and *TgAPP_{swe}^{OCN}* BMSCs with vehicle (Veh)(PBS) and 4-PBA treatment, respectively, scale bar, 20 μm. **h** Quantification of SA-β-gal⁺ cell densities in **g** (mean ± SD; *n* = 5, ***p* < 0.01, ****p* < 0.001). Two-way analysis of variance test was used in **f** and **h**.

CXCL1, 2) were increased in serum samples of *TgAPP_{swe}^{OCN}* mice treated with Veh, but decreased in the mice with D + Q treatments (Supplementary Fig. 13c, d). Together, these results suggest that the systemic inflammation in *TgAPP_{swe}^{OCN}* mice is likely in large due to the APP_{swe}-induced OB-senescence and SASPs.

Induction of ER stress-driven OB-senescence by expression of APP_{swe}, but not APP_{wt} or APP_{lon}. To understand how APP_{swe} in OB-lineage cells induces senescence, we re-analyzed the RNA-seq data (APP_{swe}⁺ vs control OB progenitors) and found that, in addition to the increases in mRNAs of senescence genes, the transcripts of ER stress genes (e.g., *Grp78*, *Atf6*, and *Hsp90*) were elevated in APP_{swe}⁺ OB-progenitor cells (Fig. 9a, b). The increase in ER stress proteins (e.g. GRP78 and ATF6) were further verified by Western blot (Fig. 9c, d). To investigate the relationship between APP_{swe}-induced ER stress and senescence, we treated APP_{swe}⁺ OB-progenitors with 4-PBA (4-Phenylbutyric acid), an inhibitor of ER stress⁵⁸. 4-PBA treatments abolished the increases of the senescence marker proteins P16^{Ink4a}, P53, and SA-β-gal (Fig. 9e–h), suggesting that APP_{swe} likely increases OB-senescence by inducing ER stress.

Notice that ER stress can be induced by the overexpression of membranous proteins⁵⁹. It thus is necessary to determine if the increased ER stress in APP_{swe}⁺ cells results from its over expression. To this end, MC3T3 cells (an OB cell line) expressing APP_{wt}-YFP (wild type), APP_{swe}-YFP, and APP_{lon}-YFP were examined. MC3T3 cells expressing APP_{swe}-YFP, but not APP_{wt}-YFP or APP_{lon}-YFP, showed an obvious increase in GRP78 (an ER stress sensor) (Supplementary Fig. 14a, b), indicating a more dramatic effect on ER stress by APP_{swe}-YFP and demonstrating its specificity.

Additionally, a more prominent co-localization of GRP78 with APP_{swe}-YFP than those with APP_{wt}-YFP or APP_{lon}-YFP was observed (Supplementary Fig. 14a, c). Moreover, APP_{swe}-YFP had an increased co-localization with EEA1, an early endosome marker, but decreased co-localization with GM130, a marker for Trans-Golgi, compared with those of APP_{wt}-YFP or APP_{lon}-YFP (Supplementary Fig. 14d–g). These results demonstrate APP_{swe}'s distinctive cellular features in its increase of GRP78 and its subcellular localizations. Finally, the senescence marker, SA-β-gal, was selectively increased in MC3T3 cells expressing APP_{swe}-YFP, but not APP_{wt} nor APP_{lon} (Supplementary Fig. 14h–i), providing additional support for the specificity of the detrimental effects by APP_{swe}, but not by the overexpression of APP_{wt} or APP_{lon}.

Discussion

Patients with AD often have osteopenia or osteoporosis^{3–10}. The lower bone mineral density is often reported in the earliest clinical stages of AD patients (both men and women) and associated with their brain atrophy and memory decline⁸. However, it remains unclear if the AD patients carrying the Swedish mutations have osteoporosis-like deficit. Here, using *TgAPP_{swe}^{OCN}* mouse model that selectively expresses APP_{swe} largely in the OB-lineage cells, we found that APP_{swe} in OB-lineage cells induces senescence and SASPs, which appear to be a key contributor of systemic inflammation, and thus promote anxiety- and depression-like behaviors in *TgAPP_{swe}^{OCN}* mice. Our studies also suggest that the senescence may be insufficient to induce the cognitive decline detected in 12-MO *TgAPP_{swe}^{OCN}* mice, which may be associated with a weak expression of APP_{swe}/Aβ₄₂ in the dDG neurons of the hippocampus. These observations, summarized in Fig. 10a, lead to a working hypothesis depicted in

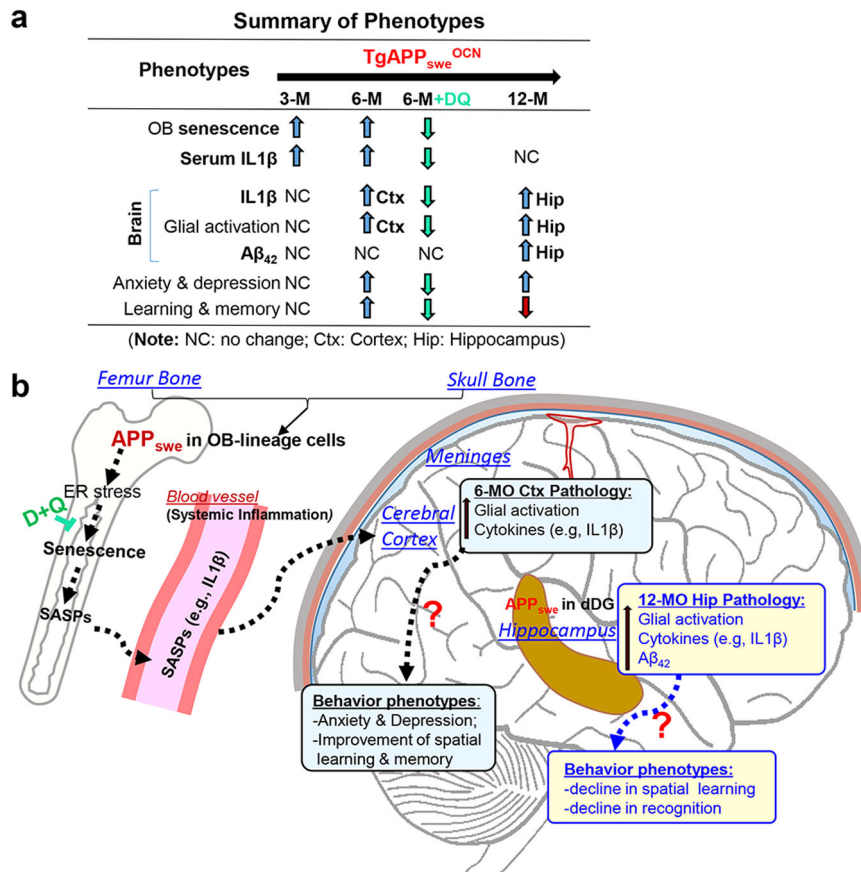


Fig. 10 Summary and working hypothesis for APP_{swe} in OB-lineage cells to regulate brain-pathology and behavior changes. **a** Summary of phenotypes detected in TgAPP_{swe}^{OCN} mice at indicated ages. **b** Illustration of the working model.

Fig. 10b, and opens a box of additional questions for future investigations.

A prerequisite to a better understanding of the mechanisms of TgAPP_{swe}^{OCN} mice' brain/behavior phenotypes is to reveal where exactly the APP_{swe} is expressed. TgAPP_{swe}^{OCN} mice are generated by crossing OCN-Cre with the LSL-hAPP_{swe} mice, and thus the APP_{swe} expression is controlled not only by the CAG promoter in LSL-hAPP_{swe} mice (for its mRNA expression), and but also by the OCN-Cre dependent removal of LSL (for hAPP_{swe} protein expression)²³. Although OCN-Cre mice express Cre largely in OB-lineage cells⁶⁰, our recent study demonstrates the Cre activity in neurons at the dDG, olfactory bulb, and cerebellum of the brain in OCN-Cre mice²⁹. Our further studies in this paper lead us to conclude that hAPP_{swe} or OCN-Cre is largely expressed in the OB-lineage cells, but weakly expressed in the dDG neurons, in 12-MO TgAPP_{swe}^{OCN} mice (Fig. 1b–g). We thus believe that the cortical brain and behavior phenotypes in 6-MO TgAPP_{swe}^{OCN} mice are likely induced by the APP_{swe} in OB-lineage cells. However, it is possible that the weak APP_{swe}/Aβ₄₂ expression in aged (12-MO) dDG hippocampal neurons contributes to the inflammation phenotypes in the mutant hippocampus and the cognitive decline (Fig. 10b).

How does APP_{swe} in OB-lineage cells induce brain pathology? Several lines of evidence support the hypothesis that APP_{swe}-induced OB-senescence and SASPs may underlie its effects on the brain, particularly the cortex, via systemic inflammation (Fig. 10b). Many SASP-like proteins were induced in cultured APP_{swe}⁺ OB progenitors and increased in serum samples of TgAPP_{swe}^{OCN} mice (Figs. 5 and 8). Cultured APP_{swe}⁺ OB progenitors and MC3T3 cells showed increased senescence cells (Fig. 6 and Supplementary Fig. 14h–i)^{52,61}. While the OB-

senescence phenotypes were temporally associated with APP_{swe}-induced bone-deficits²³, they occurred earlier than brain deficits, in TgAPP_{swe}^{OCN} mice (Fig. 6). The inhibition of senescence in TgAPP_{swe}^{OCN} mice diminished nearly all the brain and behavior phenotypes (Fig. 7 and Supplementary Fig. 12). In line with this hypothesis are the multiple literature reports that demonstrate cellular senescence as tightly linked to skeleton and brain aging and various degenerative diseases, including AD^{62–67}, and the use of senolytic drugs to attenuate the disease process has been shown in several animal models of AD^{68,69}.

In terms of the systemic inflammation, while it can be induced by deficits in multiple organs, our results suggest that APP_{swe}-induced senescence and SASPs in OB-lineage cells appear to be a key contributor to this event. Many (31 over 49, ~63%) upregulated SASP-like factors detected in serum samples of TgAPP_{swe}^{OCN} mice were also detected in Tg2576 mice (Fig. 8f). Although APP_{swe} is weakly expressed in the dDG neurons of TgAPP_{swe}^{OCN} mice (Fig. 1), examining the serum inflammatory cytokines and chemokines in mice (LSL-APP_{swe}) injected with AAV-CaMKII-Cre or AAV-GFP into their dDGs showed an increase in APP_{swe}/Aβ₄₂ in the hippocampus of Cre injected mice (Supplementary Fig. 8g), but a comparable level of serum cytokines and chemokines between Cre and GFP injected mice (Supplementary Fig. 13a, b). Treatments with senescence inhibitors (D + Q) abolished nearly all the increased inflammatory cytokines in the serum samples of TgAPP_{swe}^{OCN} mice (Supplementary Fig. 13c, d). These results thus eliminate the possible contribution of the APP_{swe}/Aβ₄₂ at the dDG to systematic inflammation, and support the view.

How does APP_{swe} in OB-lineage cells induce senescence and SASPs? We believe that APP_{swe}-induced ER stress may underlie this process for the following reasons. First, expressing APP_{wb}

APP_{swe} or APP_{lon} in osteoblastic cell line, MC3T3 cells, results in an increased of β -gal⁺ SnCs specifically in APP_{swe}⁺, but not APP_{wt}⁺ or APP_{lon}⁺, cells (Supplementary Fig. 14h–i), although APP or A β levels were increased in all three types of cells. These results not only suggest the specificity of APP_{swe} in the induction of the senescence, but also implicate A β 's insufficiency or interdependency to this event. Second, APP_{swe}, compared to APP_{wt} or APP_{lon}, exhibited distinctive features in its subcellular localizations and its induction of ER-stress, in addition to senescence (Supplementary Fig. 14a–g), revealing an association between the selective induction of the ER stress and senescence by APP_{swe}, but not APP_{wt} or APP_{lon}, in line with the view that APP_{swe} is processed by β -secretase or BACE1 in Golgi-derived vesicles, and APP_{wt} is cleaved in the endosomes⁷⁰. Third, both RNA-seq and Western blot analyses showed that APP_{swe}⁺ OB progenitors have increased expressions of not only senescence associated genes, but also ER stress genes (e.g., *Grp78*, *Atf6*, and *Hsp90*) (Fig. 9a–d); and treatment of APP_{swe}⁺ OB progenitors with an ER stress inhibitor 4-PBA abolished the increase of senescence marker proteins P16^{Ink4a}, P53, and β -gal⁺ SnCs (Fig. 9e–h), supporting the view for ER stress as a driver of senescence. Notice that Hashimoto et al. report an absence of ER stress responses in *App*^{NL-G-F} (*App* knock-in mice harboring Swedish mutation) brain⁵⁹. We thus speculate that this event may be cell type/tissue specific, and OB-lineage cells may be more sensitive to APP_{swe} than neurons in its induction of ER stress.

Are senescence and SASPs induced by osteoblastic APP_{swe} involved in the behavior changes observed in TgAPP_{swe}^{OCN} mice? Our results suggest that they are likely contributors to anxiety and depression, but insufficient to cause cognitive decline. In addition to the temporal association between the increased SASPs and the behavior changes, inhibition of senescence and SASPs by D + Q diminishes nearly all the behavior changes in TgAPP_{swe}^{OCN} mice at 6-MO (Fig. 7). Among the SASPs induced by APP_{swe}, IL-1 β is noteworthy, because IL-1 β is found to mediate bi-functions in regulating spatial learning and memory^{71–73}. Expressing IL-1 β in the brain (in particular, the cortex) exhibits enhanced spatial learning and memory in young adult, but not aged, mice⁷⁴, a similar behavioral phenotype examined in the TgAPP_{swe}^{OCN} mice (Figs. 2g and 4 and Supplementary Fig. 5g). This IL-1 β 's function is also in agreement with numerous reports, that IL-1 β is upregulated by long term potentiation (LTP) (an event critical for learning and memory)^{75–77}. The overexpression of IL-1ra, an endogenous IL-1R antagonist or IL-1R KO (knock-out), blocks spatial memory^{78,79} as well as LTP^{73,80}. In the light of these reports, we speculate that the osteoblastic APP_{swe}, via increasing IL-1 β , a key SASP, may improve hippocampal/cortex-dependent spatial learning and memory function in an age-dependent manner. We are also aware of controversial reports, which claim that IL-1 β plays a detrimental role in regulating learning and memory^{81,82}. While IL-1 β plays a role in modulating learning and memory, its precise function appears to strongly depend on the site of IL-1 β injection/increase, timing, and dosage^{73,79}. Notice that *Il1b* was increased in the hippocampus but not the cortex of 12-MO TgAPP_{swe}^{OCN} mice (Supplementary Fig. 5g–h); and such IL-1 β increase was accompanied by elevated A β ₄₂ and glial activation in the hippocampus, and cognitive decline behaviors (Supplementary Figs. 1b and 5 and Fig. 4g–i). We thus speculate that the hippocampal inflammation phenotype may be induced by the weak APP_{swe}/A β ₄₂ expression in dDG hippocampal neurons, which may also impair cognitive function in 12-MO TgAPP_{swe}^{OCN} mice (Fig. 10b). It would be of interest to further test this view in future experiments.

Finally, it is highly possible that complex mechanisms underlie APP_{swe} regulation of brain and behavior phenotypes in TgAPP_{swe}^{OCN} mice. In addition to IL-1 β and TNF α , other SASPs and growth

factors may also contribute to the brain pathology. In addition to senescence and SASPs, the weak expression of APP_{swe}/A β ₄₂ in the OCN-Cre⁺ dDG neurons may be exacerbated by systemic inflammation and be responsible for the hippocampal pathology and cognitive decline in aged (e.g., 12-MO) TgAPP_{swe}^{OCN} mice. It is also noteworthy that while chronic inflammation is believed to be one of the environmental risk factors for AD development^{30,83}, our studies suggest that the chronic systemic inflammation associated with AD patients (either EOAD or LOAD) may be induced by a combination of AD genetic risk gene(s), a primary hit, and environmental risk factors (e.g., aging, infection), a secondary hit, in line with the two-hit hypothesis⁸⁴. Further investigations that address how chronic inflammation is induced, how it promotes the brain pathology and behavior changes, and what is the function/contribution of APP_{swe}/A β ₄₂ in dDG neurons to the AD development may gain more insights into the two-hit hypothesis and AD pathogenesis.

Methods

Mice. The *LSL-APP_{swe}* mice were generated using the pCCALL2 plasmid as described previously²³. In brief, the transcription of *hAPP_{swe}* in *LSL-APP_{swe}* mice is controlled by the CAG promoter, but its translation is blocked by a loxP-stop-loxP sequence²³. Thus, the expression of *hAPP_{swe}* is controlled by both the CAG promoter and the Cre-dependent removal of LSL. The *OCN-Cre* mice were kindly provided by Tom Clemens (Johns Hopkins Medical School). *OCN-Cre*; *Ai9* and *TgAPP_{swe}^{OCN}*; *Ai9* mice were generated by crossing *Ai9* mice (from the Jackson Laboratory, donated by Dr. Hongkui Zeng, Allen Institute for Brain Science) with *OCN-Cre* and *TgAPP_{swe}^{OCN}* mice, respectively. *Ai9* mice have a loxP-flanked STOP cassette preventing the translation of a CAG promoter-driven red fluorescent protein variant (tdTomato). Thus, tdTomato is expressed following Cre-mediated recombination. The *Tg2576* mice were purchased from Taconic, Hudson, NY, USA, which express human *APP695* with Swedish double mutations at KM670/671NL (*APP_{swe}*) under the control of a hamster prion promoter²⁴. *5xFAD* transgenic mice were obtained from The Jackson Laboratory (MMRRC stock #34 840-JAX)²⁵ which express human *APP* and *PSEN1* transgenes with five AD-linked mutations (the Swedish [K670N/M671L], Florida [I716V], and London [V717I] mutation in *APP*, and the M146L and L286V mutation in *PSEN1*) under the control of mouse *Thy1* promoter. All mouse lines were backcrossed into *C57BL/6* background and housed in a room with a 12 h light/dark cycle and ad libitum access to water and rodent chow diet (Harlan Teklad S-2335). Control littermates were used in parallel for each experiment. All experimental procedures were approved by the Institutional Animal Care and Use Committee at Case Western Reserve University (IACUC, 2017–0121), according to the United States National Institutes of Health guidelines.

Antibodies and chemicals. The following primary antibodies were used and purchased as indicated below: Anti-hAPP (6E10, 803001, mouse) and anti-6E10 (Alexa Fluor[®] 647 anti- β -Amyloid, 1-16 Antibody, cat#803021) from biogen (San Diego, California, USA); Anti-Amyloid Fibrils OC antibody (AB2286, rabbit) from EMD Millipore (Temecula, California, USA); Anti-DCX (SC-8066, goat) from Santa Cruz Biotech (Santa Cruz, California, USA); Anti-Ctip2 (ab18465, Rat), anti-IBA1 (ab178846, rabbit and ab5076, goat), anti-P16^{Ink4a} (ab211542, rabbit), and anti-P53 (ab26, mouse) from Abcam (Cambridge, Massachusetts, USA); Anti-S100 β (287004, Guinea pig) from Synaptic System (Göttingen, Germany); Anti-Olig2 (p21954, rabbit), anti-GRP78 (PA1-014A, rabbit) and anti-EEA1 (PA1-063A, rabbit) from Invitrogen (Carlsbad, California, USA); Anti-ATF6 (NBP1-40256, mouse) from Novus biologicals (Centennial, CO, USA); anti-GM130 (610822, mouse) from BD biosciences (San Jose, CA, USA) and Anti-P21 (2947S, rabbit), anti-NEUN (12943S, rabbit), anti-GFAP (12389S, rabbit), and anti-GAPDH (97166S, mouse) from cell signaling (Danvers, Massachusetts, USA). Secondary antibodies were purchased from Jackson ImmunoResearch Laboratories (West Grove, Pennsylvania, USA). Dasatinib was from LC Laboratories (Woburn, MA, USA). Quercetin, polyethylene glycol 400, 4-PBA, DMSO, DAPI, and d 5-ethynyl-2'-deoxyuridine (EdU, a modified thymidine analogue that is incorporated into the DNA of dividing cells) were from Sigma Aldrich (St. Louis, MO, USA). All chemicals and reagents used in this study were of analytical grade.

Immunofluorescence staining and image analysis. Immunostaining was performed as described previously²⁹. In brief, mice were anesthetized with isoflurane and were transcardially perfused with PBS (50 mL) followed by 4% (w/v) paraformaldehyde (PFA) in phosphate buffer (PBS) (pH 7.4) (50 mL) to remove intravascular plasma proteins. The dissected brains were post-fixed in 4% PFA at 4°C overnight. Coronal sections (40 μ m) were washed 3 times with PBS (10 min each) and treated with blocking reagent (10% Donkey Serum + 0.5% Triton 100 \times) for

1 h, then incubated overnight at 4 °C with the primary antibody. Sections were washed 3 times and incubated with corresponding conjugated secondary antibody for 1 h. DAPI was used for nucleus counter staining. Stained sections were imaged by confocal microscope at room temperature. Fluorescent quantification was performed using ZEN software according to the manufacturer's instructions (Carl Zeiss).

Western blotting. Western blotting was performed as described previously⁸⁵. Brain tissues and cultured BMSCs were homogenized in modified RIPA buffer (50 mM Tris-HCl, pH 7.5, 150 mM NaCl, 1 mM EDTA) containing 0.5% sodium deoxycholate, 0.1% SDS, 1 mM PMSF, 1 mM Na₃VO₄, 1 mM NaF, 1 mM DTT, and protease inhibitor cocktail (Millipore, 539134). Lysates were centrifuged at 10,000 × g for 10 min at 4 °C to remove debris and to obtain homogenates. Samples were resolved by SDS-PAGE and transferred to a nitrocellulose membrane (1620112, Bio-Rad Laboratories). After incubation with 5% milk in TBST (10 mM Tris, 150 mM NaCl, and 0.5% Tween 20, pH 8.0) for 1 h, membranes were immunoblotted with indicated antibodies overnight at 4 °C. Membranes were washed with TBST three times and incubated with a 1:2000 dilution of horseradish peroxidase-conjugated anti-mouse or anti-rabbit antibodies for 1 h. Blots were washed with TBST three times and immunoreactive bands were visualized using the LI-COR Odyssey infrared imaging system. Intensity of immunoreactive bands were quantitated by using ImageJ (NIH).

EdU injection and labeling. Control (*LSL-APP^{swe}*) and *TgAPP^{swe}OCN* mice were given four intraperitoneal injections of EdU (50 mg/kg/time, 1 time/4 h) within 12 h. 12 hours after their last injection, mice were euthanized and transcardially perfused first with 50 ml of cold PBS and then with 50 ml of 4% PFA. The dissected brains were post-fixed in 4% PFA at 4 °C overnight. Coronal sections (40 μm) were obtained for staining. Cultured BMSCs were incubated with 10 μM EdU for 2 hours, and then cells were fixed with 4%PFA for 10 min. EdU staining was performed using a Clik-iT EdU imaging kit with Alexa-Fluor 488 (Invitrogen) following the manufacturer's instructions.

Behavioral tests. Mice (male) at ages of 3-, 6- or 12-MO (month old) were subjected to behavioral studies. Behavioral tests were done blind to genotypes or treatments. For all behavioral experiments, mice were transferred to the testing room 4 h before any test to acclimate to the environment. All behavioral instruments were cleaned with 70% ethanol prior to each trial.

Open field test (OFT), Elevated plus maze test (EPMT), and Light/dark transition test (LDT) were performed as described previously²⁹. In brief, for OFT, each mouse was placed in a chamber ($L \times W \times H = 50 \times 50 \times 20$ cm) and its movement was monitored for 10 min using an overhead camera. Light intensity was about 150 lux. The video was analyzed by a tracking software (Etho Vision, Noldus). The total distance and center (25 × 25 cm) duration time were quantified. For elevated plus maze test (EPMT), the EPM was placed 50 cm above the ground. Each mouse was initially placed in the center square facing one of the open arms ($L \times W = 60 \times 5$ cm). Light intensity was about 100 lux. Mice movement was recorded for 5 min using an overhead camera and tracking software (Etho Vision, Noldus). The time spent in the open arms and the number of open arm entries were quantified. For light/dark transition test (LDT), mouse was firstly placed in the dark compartment, overhead camera was turned on, and the door between lit and dark chambers was opened. Light intensity was about 200 lux in the lit chamber. 10 min of movement was recorded using a tracking software ((Etho Vision, Noldus). The time spent in the lit chamber and the number of transitions were quantified.

The tail suspension test (TST), forced swimming test (FST), and sucrose preference test (SPT) were performed as described previously⁸⁶. For the TST and FST, the last 4-min of a 6-min test were analyzed, and the immobility time was measured directly. The sucrose preference test was carried out using a two-bottle choice procedure. Single housed mice were habituated to drink 2% (wt/vol) sucrose solution (dissolved in water) for 3 days, then mice were given access to the two pre-weighed bottles, one containing water and the other containing 2% sucrose solution. Bottle positions were changed every day and water and sucrose solution consumption was assessed daily for 4 days. The consuming ratio of sucrose over total solution consumed was used for measuring the sucrose preference.

The Morris water maze (MWM) was performed as previously described⁸⁷. Specifically, a 120 cm pool and 10 cm platform were used for water maze and nontoxic bright white gel (Soft Gel Paste Food Color, AmeriColor) was added to the water to make the surface opaque and to hide the escape platform (1 cm below the surface). Mice were trained for 5 days, four trials per day with 20 min interval between trials and 60 s per trial to locate the hidden platform. Eight spatial cues were placed on the pool wall, visible for mice to find the hidden platform. On the 6th day, the platform was removed, and mice were placed into the pool at a new starting position. The time spent in each platform quadrant and the number of platform-crossing within 60 s were analyzed. The swim speed and the amount of time spent in each quadrant were quantified using the video tracking system (Noldus). The investigators were blind to genotype during data acquisition and analysis.

The Novel Object Recognition Task (NOR) was based on a previous published procedure⁸⁸. It consists of a *habituation phase* followed by a *testing phase*. During the *habituation phase*, each mouse was allowed to freely explore the empty arena over two days. On the third day, the testing phase begun. Habituation consisted of one ten-minute session administered one per day. The *testing phase* consisted of a (1) *familiarization trial* followed by a (2) *test trial*. During the *familiarization trial*, a single mouse was placed in the arena containing two identical objects and released against the center of the opposite wall with its back to the objects. This was done to prevent coercion to explore the objects. Object interaction is defined as entrance into the object-containing zone resulting in direct or nearly direct object contact with the nose or whiskers. The test trials were administered after delays of 1-hour post-familiarization. The *test trial* was administered in the aforementioned way except that one sample object from the familiarization trial and one novel object were presented. During the test trials, time spent with novel object per total time with both objects as the novel object preference was quantified.

AAV virus injection. AAV9-CamkII-GFP (105541-AAV9) and AAV9-CamkII-Cre (105551-AAV9) were purchased from Addgene. Virus injection was performed as described previously²⁹. In brief, male *LSL-APP^{swe}* mice (4-month-old) were anesthetized with Ketamine/Xylazine (HENRY SCHEIN #056344), and the head was fixed in a stereotaxic device (David Kopf Instruments). After the antiseptic treatment, the skull was exposed and cleaned using 1% H₂O₂. Holes were drilled into the skull and viruses were bilaterally injected into DG at the coordinates relative to bregma: caudal: -2.06 mm; lateral: ±1.3 mm; ventral: -1.75 mm. After injection, the needle was left in place for 5 min to allow for diffusion of injected viruses before being slowly withdrawn. For the following 5 days, mice were daily injected with Meloxicam to reduce pain. Injection locations were validated in each mouse after experiments.

In vitro primary OB-progenitor (BMSCs) cultures. OB-progenitor (BMSCs) culture was carried out following a standard protocol as described previously^{28,85}. In brief, the whole bone marrow cells flushed out from long bones of mice with DMEM were filtered through a 70-μm filter mesh, washed, re-suspended, and then plated in 100-mm dishes with growth medium (DMEM plus 10% FBS), which were incubated at 37 °C with 5% CO₂. 3 days later, the non-adherent cells were removed. The attached bone marrow cells were cultured with the growth medium for 7 days. These cells were passaged and cultured for another 3–6 days with the same growth medium. These cells, so called BMSCs, were used for Western blot, RT-PCR, and SA-β-gal staining.

Flow cytometry analysis. Flow cytometry analysis was done as previously described²⁸. BMSCs were flushed from femurs and tibias of 6-MO *OCN-Cre*; *Ai9* and *TgAPP^{swe}OCN*; *Ai9* mice, the attached bone marrow cells were cultured with the growth medium for 7 days. These cells were passaged and cultured for another 3 days with the same growth medium. Then cell media were removed from culture dishes and cells were rinsed with PBS. Trypsin solution was added to incubate at 37 °C for 2 min. The detached adherent cells were centrifuged, and the pellet cells were washed with 1 ml cold PBS, and finally resuspended in 0.5 ml PBS with 1% FBS for flow cytometry analysis. Flow cytometric analysis was performed by use of a flow cytometer in CWRU core facility. Acquisition and analysis were performed by using FACSDiva 8.0.1 software (BD).

Generation of plasmids of APP_{WT}-YFP, APP_{swe}-YFP, and APP_{ion}-YFP. YFP-APP_{swe} mutation (K670N/M671L, AAG ATG - AAC TTG) and YFP-APP-London point mutation (V717I, GTC - ATC) from the YFP-APP_{WT} construct by using the Q5 Site-Directed Mutagenesis Kit (E0554S, New England Biolabs, Inc). The primers 'CTGAAGTGAAGCTGGATGCAGAAATCCGACATG' and 'AGATCTCCTCCGCTTGTATATTG' were used to generate the K670N/M671L mutation, and the primers 'CATCACCTTGGTATGCTGAAG' and 'ATGATCACTGTGCTATGACAAC' were used to generate the V717I point mutation.

MC3T3 cell culture and transfections of YFP, APP_{WT}-YFP, APP_{swe}-YFP, and APP_{ion}-YFP plasmids. MC3T3-E1 cells were grown in DMEM containing 10% (vol/vol) FBS, and 50 units/ml penicillin and streptomycin. Cells plated at 1 × 10⁴/well onto 12-wells coverslips the day before transfection. Cells were transfected with control-YFP Vector, APP_{WT}-YFP, APP_{swe}-YFP, and APP_{ion}-YFP by Lipofectamine 3000 (Invitrogen). Forty-eight hours after transfection, cells were subjected to SA-β-gal staining and immunofluorescence staining.

SA-β-gal staining. Cultured OB progenitors and MC3T3 cells SA-β-gal staining was performed as previously reported⁸⁵. SA-β-gal staining was performed using a SA-β-gal staining kit (Cell Signaling, #9860) according to the manufacturer's instructions.

Elisa assay for IL1β, IL6, human Aβ₄₀, and human Aβ₄₂. Blood samples were collected, allowed to clot for 30 min, and centrifuged for 10 min at 3000 rpm. Serum was frozen and aliquot at -80 °C until use. Serum IL1β was measured with Mouse IL-1 beta ELISA Kit (KE10003, Proteintech), following the manufacturers'

instruction. Serum IL-6 was measured with mouse IL-6 ELISA kit (550950, BD Biosciences), following the manufacturers' instruction. Serum, Brain and BMSCs homogenization was obtained for human A $\beta_{40/42}$ Elisa assay. Brain tissues were homogenized as previously described⁸⁷. Human A β_{40} and A β_{42} level in serum, brain (300 μ g in total protein) and BMSCs (50 μ g in total protein) homogenates were measured by the A β_{40} human ELISA kit (Invitrogen, catalog #KHB3481) and the A β_{42} human ELISA kit (Millipore, catalog #EZHS42), respectively. Their concentrations were determined by comparing readings against their standard curves.

L-Series label-multiplex antibody arrays. Mice blood samples were collected and allowed to clot for 30 min at room temperature and centrifuged for 15 min at 3000 rpm. Serum was frozen and aliquot at -80°C until use. The antibody arrays were performed using an L-Series Glass Slide antibody arrays kit (AAM-SERV-LG, Raybiotech, USA) according to the manufacturer's instructions. In brief, the serum was dialyzed before the biotin-labeling step. The primary amine of the proteins in the sample was biotinylated, followed by dialysis to remove free biotin. The newly biotinylated sample was added onto the glass slide and incubated at room temperature. After incubation with Fluorescent Dye-Streptavidin, the signals were visualized by fluorescence.

Mouse cytokine array. Serum samples were collected as described above. Cytokines were measured with Mouse Cytokine Array Panel A (ARY006, R&D Systems). In Brief, the serum was mixed with a cocktail of biotinylated detection antibodies. The sample/antibody mixture was then incubated with the Mouse Cytokine Array membrane. Any cytokine/detection antibody complex present was bound by its cognate immobilized capture antibody on the membrane. Following a wash to remove unbound material, streptavidin-horseradish peroxidase and chemiluminescent detection reagents were added sequentially. Light was produced at each spot in proportion to the amount of cytokine bound.

RNA isolation and qPCR. Total RNA was isolated from brain tissues and BMSCs by using the RNeasy Mini Kit (QIAGEN, Cat No. 74104), and purified RNA (1–5 μ g) was used for cDNA synthesis with the Revert Aid First Strand cDNA Synthesis Kit (Thermo Scientific, # K1621). cDNA products were subjected for subsequent quantitative PCR (qPCR) using the QuantiFast SYBR Green PCR Kit (204057; QIAGEN) with a qPCR System (StepOne Plus). Primers used were as follows: hAPP, 5'-GCCCTTCTCGTTCCTGAC-3' and 5'-TCGCAAACATCCATCCCTC-3'; OCN-Cre, 5'-CAAATAGCCCTGGCAGATTG-3' and 5'-TGATACAAGGACATCTTCC-3'; mAPP, 5'-TCCGTGTGATCTACGAGCGCAT-3' and 5'-GCCAAGACATCGTCGGAGTAGT-3'; Vps35, 5'-GACTTCGCTGATGAACAGAGCC-3' and 5'-CAGTGTGAAGCGAATCCGCTGA-3'; Trem2, 5'-CTACCAGTGTGAGAGTCTCCGA-3' and 5'-CCTCGAAACTCGATGACTCCTC-3'; Apoe, 5'-GAACCGCTTCTGGGATTACCTG-3' and 5'-GCCTTTACTTCCGTCATATGTC-3'; Sor11, 5'-GAACACCTGTCTCCGAAACCAG-3' and 5'-CGGAACTGAGTGTCTGCATAC-3'; Ptk2b, 5'-CTGGAGAGCATCAACTGTGTGAC-3' and 5'-GATGGGTGAGCGTGTGACAGAG-3'; Mx2, 5'-AAGACGGAGCACCGTGGATACA-3' and 5'-CGTGTGCTTGTGTTTCTCAG-3'; Runx2, 5'-CCTGAACCTGACCAAGTCT-3' and 5'-TCATCTGGCTCAGATAGGAGG-3'; Sp7 (Osterix), 5'-GGCTTTTCTGCGCAAGAGGTT-3' and 5'-CGTGTGATGTTGCTCAAGTGGTC-3'; Nfatc1, 5'-GGTGCCTTTTGGCAGCAGTATC-3' and 5'-CGTATGGACCAGAAATGTGACGG-3'; Col1a1, 5'-CCTCAGGGTATTGCTGGACAAC-3' and 5'-CAGAAGGACCTTGTTCAGAG-3'; Spp1 (Osteopontin), 5'-GCTTGGCTTATGGACTGAGGTC-3' and 5'-CCTTAGACTCACCCTCTTCATG-3'; Bglap (Osteocalcin), 5'-GCAATAAGGTAGTGAACAGACTCC-3' and 5'-CCATAGATGCGTTTGTAGGCGG-3'; Sparc (Osteonectin), 5'-CACCTGGACTACATCGGACCAT-3' and 5'-CTGCTTCTCAGTGAGGAGTTG-3'; Bmp2, 5'-TGTGAGGATTAGCAGGTCTTTC-3' and 5'-CTCGTTTGTGGAGCGGATGT-3'; Lrp4, 5'-GTGTGGCAGAACCCTTGACAGTCTC-3' and 5'-TACGGTCTGAGCCATCCATTC-3'; Ctnnb1 (beta-catenin), 5'-GTTCGCTTCAATTATGACTGCC-3' and 5'-ATAGACCCTGTTCGCCAAAAG-3'; Tnfrsf11 (Rankl), 5'-ATCCCATCGGGTCCCATAA-3' and 5'-TCCGTTGCTTAAACGTCATGTTAG-3'; Tnfrsf11b (Opg), 5'-GGCCTGATGTATGCCCTCAA-3' and 5'-GTGCAGGAACCTCATGGTCTTC-3'; Alpl, 5'-CCAGAAAGACACCTTGACTGG-3' and 5'-TCTTGTCCGTGTCGCTCACCAT-3'; Il1b, 5'-TGGACCTCCAGGATGAGGACA-3' and 5'-GTTCACTCGGAGCCCTGTAGTG-3'; Il6, 5'-CTTGGGACTGATGCTGGTG-3' and 5'-TTGGGAGTGGTATCTCTGTGA-3'; Il10, 5'-CGGAAGACAATAACTGCACCC-3' and 5'-CGGTAGCAGTATGTTGCCAGC-3'; Tnfa, 5'-GGCGGTGCTTATGTCTCA-3' and 5'-CCTCCACTTGGTGGTTGT-3'; Cxcl1, 5'-TCCAGAGCTTGAAGGTGTTGCC-3' and 5'-AACCAAGGAGCTCAGGGTCA-3'; Ccl5, 5'-ACCCTCCCTGCTGCTT-3' and 5'-ACACTGGCGGTTCTCTC-3'; Tgfb1, 5'-ACCGCAACAACGCCATCT-3' and 5'-GGGCATGCTTCCCGAAT-3'; Csf2, 5'-AACCTCCTGGATGACATGCCTG-3' and 5'-AAATGCCCCGTAGACCCTGCT-3'; Mmp3, 5'-CTCTGGAACCTGAGACATCC-3' and 5'-AGGAGTCTGAGAGATTGCGC-3'; Grp78, 5'-TGTCTTCTCAGCATCAAGCAAGG-3' and 5'-CCAACACTTCTGACAGGCTT-3'; Atf6, 5'-GTCCAAAGCGAAGAGCTGTCTG-3' and 5'-AGAGATGCCTCCTCTGATTGGC-3'; Hsp90b1, 5'-GTTTCCCGTGAGACTCTTACG-3' and 5'-ATTCGTGCCAACTCCTTCCAG-3'; Eif2ak3, 5'-CCG

ATGTCAGTGACAACAGCTG-3' and 5'-AAGACAACGCCAAAGCCACCAC-3'; Ern1, 5'-GGCTACCATATCTCTGAGCACC-3' and 5'-CTCCTTCTGGAACCTGTGGTGC-3'; Hsp90a1, 5'-GCTTTCAGAGCTGTTCGGGTAC-3' and 5'-AAAGCGGAGTTAGCAACCTGG-3'; Hspa2, 5'-GCACCTTCGATGTGCCATCCT-3' and 5'-TGGCTGACCATACGGTTGTGCA-3'; Sirt3, 5'-GCTACATGCACGGTCTGTGCAA-3' and 5'-CAATGTCGGGTTTCAACCGCC-3'; GAPDH, 5'-AAGGTCATCCACAGAGCTGAA-3' and 5'-CTGCTTACCACCTTCTTGA-3'. Each sample was repeated at least 3 times, and the mRNA level was normalized to GAPDH using the $2^{-\Delta\Delta\text{Ct}}$ method.

Bulk RNA-sequencing. Total RNAs were extracted from purified Td⁺ OB-progenitor cells from OCN-Cre; Ai9 and *TgAPP^{swe}OCN*; Ai9 mice by flow cytometer. RNA Integrity Number (RIN) was accessed for every sample, and the samples were considered qualified with RIN > 2. These RNA samples were then subjected to RNA-seq analyses by BGI America (Cambridge, MA) using the DNBSeq platform. Firstly, we removed the reads mapped to rRNA and obtained the raw data with 52.47 Mb reads. After filtering low-quality, adaptor-polluted and high content of unknown base reads in the sequencing reads, 51.9 Mb clean reads were obtained per sample on average. Then clean reads were mapped to reference genome using HISAT2. On average 92.91% reads were mapped and the uniformity of the mapping result for each sample suggests that the samples were comparable. Comparisons to RNAseq were normalized to fpkm values. DESeq2 was used and the PossonDis algorithms detected the differential expression genes (DEGs). The Benjamini and Hochberg (BH) correction was applied to adjust *p*-value. DEGs were determined with $\text{adj.P.value} \leq 0.05$ and $|\text{Log}_2 \text{fold change}| \geq 1$. Normalized RNA-seq data were provided in Supplementary Data 1. Heatmap was generated by TBtools software. Gene expression profiles were Z-transferred. Secreted protein database was obtained from <http://proteomics.yzu.edu/secretomes/animal/index.php>. Gene Ontology (GO) enrichment analysis was performed by GO database (<http://www.geneontology.org/>). GO terms with *p*-value ≤ 0.05 were defined as significantly enriched.

Statistics and reproducibility. All data were expressed as means \pm SD. For in vivo studies, three to ten male mice per genotype per assay were used. For in vitro cell biological and biochemical studies, each experiment was repeated at least three times. Statistical analyses were performed using GraphPad Prism 7.0. Mann-Whitney *U* test or unpaired Student's *t* test was used to compare data from two groups. For multiple comparisons of three or more groups of samples, ANOVA was used. The significance level was set at $P < 0.05$ (* $P < 0.05$, ** $P < 0.01$, *** $P < 0.001$).

Reporting summary. Further information on research design is available in the Nature Research Reporting Summary linked to this article.

Data availability

Source data of figures are provided in Supplementary Data 1. Sequencing data that support the findings in this study have been assigned Gene Expression Omnibus accession number GSE186827. The uncropped Western blots are provided in Supplementary Figs. 15–22. The data that support the findings of this study are available from the corresponding author upon reasonable request.

Received: 2 February 2021; Accepted: 3 November 2021;

Published online: 25 November 2021

References

- Leng, F. & Edison, P. Neuroinflammation and microglial activation in Alzheimer disease: where do we go from here? *Nat. Rev. Neurol.* **17**, 157–172 (2020).
- Wang, J., Gu, B. J., Masters, C. L. & Wang, Y. J. A systemic view of Alzheimer disease—insights from amyloid-beta metabolism beyond the brain. *Nat. Rev. Neurol.* **13**, 612–623 (2017).
- Basgoz, B., Ince, S., Safer, U., Naharci, M. I. & Tasci, I. Low bone density and osteoporosis among older adults with Alzheimer's disease, vascular dementia, and mixed dementia: a cross-sectional study with prospective enrollment. *Turkish J. Phys. Med. Rehabil.* **66**, 193–200 (2020).
- Mjoberg, B., Hellquist, E., Mallmin, H. & Lindh, U. Aluminum, Alzheimer's disease and bone fragility. *Acta Orthopaedica Scandinavica* **68**, 511–514 (1997).
- Frame, G., Bretland, K. A. & Dengler-Crish, C. M. Mechanistic complexities of bone loss in Alzheimer's disease: a review. *Connect. Tissue Res.* **61**, 4–18 (2020).
- Zhou, R., Zhou, H., Rui, L. & Xu, J. Bone loss and osteoporosis are associated with conversion from mild cognitive impairment to Alzheimer's disease. *Curr. Alzheimer Res.* **11**, 706–713 (2014).

7. O'Mahony, D. et al. Bone aluminium content in Alzheimer's disease. *Dementia* **6**, 69–72 (1995).
8. Loskutova, N., Honea, R. A., Vidoni, E. D., Brooks, W. M. & Burns, J. M. Bone density and brain atrophy in early Alzheimer's disease. *J. Alzheimer's Dis.* **18**, 777–785 (2009).
9. Zhou, R., Deng, J., Zhang, M., Zhou, H. D. & Wang, Y. J. Association between bone mineral density and the risk of Alzheimer's disease. *J. Alzheimers Dis.* **24**, 101–108 (2011).
10. Sinha, U. K., Saadat, D., Linthicum, F. H. Jr., Hollen, K. M. & Miller, C. A. Temporal bone findings in Alzheimer's disease. *Laryngoscope* **106**, 1–5 (1996).
11. Paloneva, J. et al. DAP12/TREM2 deficiency results in impaired osteoclast differentiation and osteoporotic features. *J. Exp. Med.* **198**, 669–675 (2003).
12. Takahashi, K., Rochford, C. D. & Neumann, H. Clearance of apoptotic neurons without inflammation by microglial triggering receptor expressed on myeloid cells-2. *J. Exp. Med.* **201**, 647–657 (2005).
13. Yeh, F. L., Hansen, D. V. & Sheng, M. TREM2, microglia, and neurodegenerative diseases. *Trends Mol. Med.* **23**, 512–533 (2017).
14. Otero, K. et al. TREM2 and beta-catenin regulate bone homeostasis by controlling the rate of osteoclastogenesis. *J. Immunol.* **188**, 2612–2621 (2012).
15. Ulland, T. K. & Colonna, M. TREM2 - a key player in microglial biology and Alzheimer disease. *Nat. Rev. Neurol.* **14**, 667–675 (2018).
16. Belloy, M. E., Napolioni, V. & Greicius, M. D. A quarter century of APOE and Alzheimer's disease: progress to date and the path forward. *Neuron* **101**, 820–838 (2019).
17. Zajickova, K., Zofkova, I., Hill, M., Horinek, A. & Novakova, A. Apolipoprotein E 4 allele is associated with low bone density in postmenopausal women. *J. Endocrinol. Investig.* **26**, 312–315 (2003).
18. Peter, I. et al. Associations of APOE gene polymorphisms with bone mineral density and fracture risk: a meta-analysis. *Osteoporos. Int.* **22**, 1199–1209 (2011).
19. Hardy, J. A hundred years of Alzheimer's disease research. *Neuron* **52**, 3–13 (2006).
20. Hardy, J. Has the amyloid cascade hypothesis for Alzheimer's disease been proved? *Curr. Alzheimer Res.* **3**, 71–73 (2006).
21. Hardy, J. Alzheimer's disease: the amyloid cascade hypothesis: an update and reappraisal. *J. Alzheimers Dis.* **9**, 151–153 (2006).
22. Cui, S. et al. APP^{swe}/Abeta regulation of osteoclast activation and RAGE expression in an age-dependent manner. *J. Bone Min. Res.* **26**, 1084–1098 (2011).
23. Xia, W. F. et al. Swedish mutant APP suppresses osteoblast differentiation and causes osteoporotic deficit, which are ameliorated by N-acetyl-L-cysteine. *J. Bone Min. Res.* **28**, 2122–2135 (2013).
24. Hsiao, K. et al. Correlative memory deficits, Abeta elevation, and amyloid plaques in transgenic mice. *Science* **274**, 99–102 (1996).
25. Oakley, H. et al. Intraneuronal beta-amyloid aggregates, neurodegeneration, and neuron loss in transgenic mice with five familial Alzheimer's disease mutations: potential factors in amyloid plaque formation. *J. Neurosci.* **26**, 10129–10140 (2006).
26. Pan, J. X. et al. APP promotes osteoblast survival and bone formation by regulating mitochondrial function and preventing oxidative stress. *Cell Death Dis.* **9**, 1077 (2018).
27. Zhang, J. & Link, D. C. Targeting of mesenchymal stromal cells by Cre-recombinase transgenes commonly used to target osteoblast lineage cells. *J. Bone Miner. Res.* **31**, 2001–2007 (2016).
28. Pan, J. X. et al. YAP promotes osteogenesis and suppresses adipogenic differentiation by regulating beta-catenin signaling. *Bone Res.* **6**, 18 (2018).
29. Sun, D. et al. Critical roles of embryonic born dorsal dentate granule neurons for activity-dependent increases in BDNF, adult hippocampal neurogenesis, and antianxiety-like behaviors. *Biol. Psychiatry* **89**, 600–614 (2020).
30. Akiyama, H. et al. Inflammation and Alzheimer's disease. *Neurobiol. Aging* **21**, 383–421 (2000).
31. Fakhoury, M. Microglia and astrocytes in Alzheimer's Disease: implications for therapy. *Curr. Neuropharmacol.* **16**, 508–518 (2018).
32. Wirths, O. Altered neurogenesis in mouse models of Alzheimer disease. *Neurogenesis* **4**, e1327002 (2017).
33. Miller, A. H. & Raison, C. L. The role of inflammation in depression: from evolutionary imperative to modern treatment target. *Nat. Rev. Immunol.* **16**, 22–34 (2016).
34. Singhal, G. & Baune, B. T. Microglia: an interface between the loss of neuroplasticity and depression. *Front. Cell. Neurosci.* **11**, 270 (2017).
35. Hill, A. S., Sahay, A. & Hen, R. Increasing adult hippocampal neurogenesis is sufficient to reduce anxiety and depression-like behaviors. *Neuropsychopharmacology* **40**, 2368–2378 (2015).
36. Revest, J. M. et al. Adult hippocampal neurogenesis is involved in anxiety-related behaviors. *Mol. Psychiatry* **14**, 959–967 (2009).
37. Hanson, N. D., Owens, M. J. & Nemeroff, C. B. Depression, antidepressants, and neurogenesis: a critical reappraisal. *Neuropsychopharmacology* **36**, 2589–2602 (2011).
38. Rossi, S. et al. Neuroinflammation drives anxiety and depression in relapsing-remitting multiple sclerosis. *Neurology* **89**, 1338–1347 (2017).
39. Bailey, K. R. & Crawley, J. N. in *Methods of Behavior Analysis in Neuroscience* (eds. nd & Buccafusco, J. J.) (Boca Raton, 2009).
40. Belovicova, K., Bogi, E., Csatoslova, K. & Dubovicky, M. Animal tests for anxiety-like and depression-like behavior in rats. *Interdiscip. Toxicol.* **10**, 40–43 (2017).
41. Nie, L. et al. Melatonin ameliorates anxiety and depression-like behaviors and modulates proteomic changes in triple transgenic mice of Alzheimer's disease. *BioFactors* **43**, 593–611 (2017).
42. Nyarko, J. N. K., Quartey, M. O., Baker, G. B. & Mousseau, D. D. Can animal models inform on the relationship between depression and Alzheimer disease? *Can. J. Psychiatry Rev. Canadienne de. Psychiatr.* **64**, 18–29 (2019).
43. Espana, J. et al. Intraneuronal beta-amyloid accumulation in the amygdala enhances fear and anxiety in Alzheimer's disease transgenic mice. *Biol. Psychiatry* **67**, 513–521 (2010).
44. Cerejeira, J., Lagarto, L. & Mukaetova-Ladinska, E. B. Behavioral and psychological symptoms of dementia. *Front. Neurol.* **3**, 73 (2012).
45. Starkstein, S. E., Jorge, R., Mizrahi, R. & Robinson, R. G. The construct of minor and major depression in Alzheimer's disease. *Am. J. Psychiatry* **162**, 2086–2093 (2005).
46. Ismail, Z. et al. Neuropsychiatric symptoms as early manifestations of emergent dementia: provisional diagnostic criteria for mild behavioral impairment. *Alzheimer's Dement.* **12**, 195–202 (2016).
47. Chapman, P. F. et al. Impaired synaptic plasticity and learning in aged amyloid precursor protein transgenic mice. *Nat. Neurosci.* **2**, 271–276 (1999).
48. Xia, D. et al. Presenilin-1 knockin mice reveal loss-of-function mechanism for familial Alzheimer's disease. *Neuron* **85**, 967–981 (2015).
49. Vorhees, C. V. & Williams, M. T. Morris water maze: procedures for assessing spatial and related forms of learning and memory. *Nat. Protoc.* **1**, 848–858 (2006).
50. Antunes, M. & Biala, G. The novel object recognition memory: neurobiology, test procedure, and its modifications. *Cogn. Process.* **13**, 93–110 (2012).
51. Reger, M. L., Hovda, D. A. & Giza, C. C. Ontogeny of rat recognition memory measured by the novel object recognition task. *Dev. Psychobiol.* **51**, 672–678 (2009).
52. Young, A. R. & Narita, M. SASP reflects senescence. *EMBO Rep.* **10**, 228–230 (2009).
53. Martinez, D. E. et al. SASP, a Senescence-Associated Subtilisin Protease, is involved in reproductive development and determination of silique number in Arabidopsis. *J. Exp. Bot.* **66**, 161–174 (2015).
54. Mirzayans, R., Andrais, B., Scott, A., Paterson, M. C. & Murray, D. Single-cell analysis of p16(INK4a) and p21(WAF1) expression suggests distinct mechanisms of senescence in normal human and Li-Fraumeni Syndrome fibroblasts. *J. Cell. Physiol.* **223**, 57–67 (2010).
55. Kang, C. et al. The DNA damage response induces inflammation and senescence by inhibiting autophagy of GATA4. *Science* **349**, aaa5612 (2015).
56. Kirkland, J. L. & Tchkonina, T. Senolytic drugs: from discovery to translation. *J. Intern. Med.* **288**, 518–536 (2020).
57. Zhu, Y. et al. The Achilles' heel of senescent cells: from transcriptome to senolytic drugs. *Aging Cell* **14**, 644–658 (2015).
58. Pao, H. P. et al. Suppression of endoplasmic reticulum stress by 4-PBA protects against hyperoxia-induced acute lung injury via up-regulating claudin-4 expression. *Front. Immunol.* **12**, 674316 (2021).
59. Hashimoto, S. et al. Endoplasmic reticulum stress responses in mouse models of Alzheimer's disease: overexpression paradigm versus knockin paradigm. *J. Biol. Chem.* **293**, 3118–3125 (2018).
60. Zhang, M. et al. Osteoblast-specific knockout of the insulin-like growth factor (IGF) receptor gene reveals an essential role of IGF signaling in bone matrix mineralization. *J. Biol. Chem.* **277**, 44005–44012 (2002).
61. McCormick, A. & Campisi, J. Cellular aging and senescence. *Curr. Opin. Cell Biol.* **3**, 230–234 (1991).
62. Raskin, N. & Ehrenberg, R. Senescence, senility, and Alzheimer's disease. *Am. J. Psychiatry* **113**, 133–137 (1956).
63. Boccardi, V., Pelini, L., Ercolani, S., Ruggiero, C. & Mecocci, P. From cellular senescence to Alzheimer's disease: the role of telomere shortening. *Ageing Res Rev.* **22**, 1–8 (2015).
64. Charlesworth, B. Evolution of senescence: Alzheimer's disease and evolution. *Curr. Biol.* **6**, 20–22 (1996).
65. Han, X., Zhang, T., Liu, H., Mi, Y. & Gou, X. Astrocyte senescence and Alzheimer's disease: a review. *Front. Aging Neurosci.* **12**, 148 (2020).
66. Bryant, A. G. et al. Cerebrovascular senescence is associated with Tau pathology in Alzheimer's disease. *Front. Neurol.* **11**, 575953 (2020).
67. Farr, J. N. et al. Targeting cellular senescence prevents age-related bone loss in mice. *Nat. Med.* **23**, 1072–1079 (2017).
68. Musi, N. et al. Tau protein aggregation is associated with cellular senescence in the brain. *Aging Cell* **17**, e12840 (2018).

69. Zhang, P. et al. Senolytic therapy alleviates Abeta-associated oligodendrocyte progenitor cell senescence and cognitive deficits in an Alzheimer's disease model. *Nat. Neurosci.* **22**, 719–728 (2019).
70. Haass, C. et al. The Swedish mutation causes early-onset Alzheimer's disease by beta-secretase cleavage within the secretory pathway. *Nat. Med.* **1**, 1291–1296 (1995).
71. Huang, Z. B. & Sheng, G. Q. Interleukin-1beta with learning and memory. *Neurosci. Bull.* **26**, 455–468 (2010).
72. Donzis, E. J. & Tronson, N. C. Modulation of learning and memory by cytokines: signaling mechanisms and long term consequences. *Neurobiol. Learn. Mem.* **115**, 68–77 (2014).
73. Goshen, I. et al. A dual role for interleukin-1 in hippocampal-dependent memory processes. *Psychoneuroendocrinology* **32**, 1106–1115 (2007).
74. Takemiya, T., Fumizawa, K., Yamagata, K., Iwakura, Y. & Kawakami, M. Brain Interleukin-1 facilitates learning of a water maze spatial memory task in young mice. *Front. Behav. Neurosci.* **11**, 202 (2017).
75. Balschun, D. et al. Hippocampal interleukin-1 beta gene expression during long-term potentiation decays with age. *Ann. N. Y. Acad. Sci.* **992**, 1–8 (2003).
76. del Rey, A., Balschun, D., Wetzell, W., Randolph, A. & Besedovsky, H. O. A cytokine network involving brain-borne IL-1beta, IL-1ra, IL-18, IL-6, and TNFalpha operates during long-term potentiation and learning. *Brain, Behav., Immun.* **33**, 15–23 (2013).
77. Schneider, H. et al. A neuromodulatory role of interleukin-1beta in the hippocampus. *Proc. Natl Acad. Sci. USA* **95**, 7778–7783 (1998).
78. Spulber, S. et al. Impaired long term memory consolidation in transgenic mice overexpressing the human soluble form of IL-1ra in the brain. *J. Neuroimmunol.* **208**, 46–53 (2009).
79. Yirmiya, R., Winocur, G. & Goshen, I. Brain interleukin-1 is involved in spatial memory and passive avoidance conditioning. *Neurobiol. Learn. Mem.* **78**, 379–389 (2002).
80. Ross, F. M., Allan, S. M., Rothwell, N. J. & Verkhratsky, A. A dual role for interleukin-1 in LTP in mouse hippocampal slices. *J. Neuroimmunol.* **144**, 61–67 (2003).
81. Moore, A. H., Wu, M., Shaftel, S. S., Graham, K. A. & O'Banion, M. K. Sustained expression of interleukin-1beta in mouse hippocampus impairs spatial memory. *Neuroscience* **164**, 1484–1495 (2009).
82. Loscher, C. E., Mills, K. H. & Lynch, M. A. Interleukin-1 receptor antagonist exerts agonist activity in the hippocampus independent of the interleukin-1 type I receptor. *J. Neuroimmunol.* **137**, 117–124 (2003).
83. Kinney, J. W. et al. Inflammation as a central mechanism in Alzheimer's disease. *Alzheimer's Dement.* **4**, 575–590 (2018).
84. Zhu, X., Raina, A. K., Perry, G. & Smith, M. A. Alzheimer's disease: the two-hit hypothesis. *Lancet Neurol.* **3**, 219–226 (2004).
85. Xiong, L. et al. Linking skeletal muscle aging with osteoporosis by lamin A/C deficiency. *PLoS Biol.* **18**, e3000731 (2020).
86. Sun, D. et al. Neogenin, a regulator of adult hippocampal neurogenesis, prevents depressive-like behavior. *Cell Death Dis.* **9**, 8 (2018).
87. Zhang, H. et al. A role of Low-Density Lipoprotein Receptor-Related Protein 4 (LRP4) in astrocytic abeta clearance. *J. Neurosci.* **40**, 5347–5361 (2020).
88. Ennaceur, A. & Delacour, J. A new one-trial test for neurobiological studies of memory in rats. I: behavioral data. *Behav. Brain Res.* **31**, 47–59 (1988).

Acknowledgements

We thank members in MeiXiong laboratories for helpful discussions, suggestions, and technical help. This study is supported in part by the National Institutes of Health (AG045781, AG051773, and AG051510 to W.-C.X.) and the Department of Veterans Administration (to W.-C.X.). We also thank Meisel Family and InMotion at Cleveland, Ohio.

Author contributions

J.P. and W.-C.X. designed the project and wrote the manuscript. J.P. and D.S. performed behavioral tests, virus injection, immunostaining, Western blot, and data analysis. D.L. performed MWM tests and data quantification. X.R. performed RNA-seq data analysis. L.X. generated the plasmids encoding APP_{lon}-YFP and APP_{swe}-YFP and did transfection of MC3T3 cells and data analysis; H.G. did L-Series label-multiplex antibody arrays. L.Y. helped with virus injection and data analysis. Y.L. performed mice genotyping and kept mouse lines. C.J. performed BMSCs culture. W.-C.X. helped data analysis, interpretation, and supervised the project.

Competing interests

The authors declare no competing interests.

Additional information

Supplementary information The online version contains supplementary material available at <https://doi.org/10.1038/s42003-021-02843-2>.

Correspondence and requests for materials should be addressed to Wen-Cheng Xiong.

Peer review information *Communications Biology* thanks the anonymous reviewers for their contribution to the peer review of this work. Primary Handling Editors: Martina Rauner and Karli Montague-Cardoso. Peer reviewer reports are available.

Reprints and permission information is available at <http://www.nature.com/reprints>

Publisher's note Springer Nature remains neutral with regard to jurisdictional claims in published maps and institutional affiliations.



Open Access This article is licensed under a Creative Commons Attribution 4.0 International License, which permits use, sharing, adaptation, distribution and reproduction in any medium or format, as long as you give appropriate credit to the original author(s) and the source, provide a link to the Creative Commons license, and indicate if changes were made. The images or other third party material in this article are included in the article's Creative Commons license, unless indicated otherwise in a credit line to the material. If material is not included in the article's Creative Commons license and your intended use is not permitted by statutory regulation or exceeds the permitted use, you will need to obtain permission directly from the copyright holder. To view a copy of this license, visit <http://creativecommons.org/licenses/by/4.0/>.

© The Author(s) 2021